SYNTHESIS OF HOLLOW HYDROXYAPATITE PARTICLES FOR ORHOPEDIC APPLICATIONS

A THESIS SUBMITTED TO
THE GRADUATE SCHOOL OF NATURAL AND APPLIED SCIENCES
OF
MIDDLE EAST TECHNICAL UNIVERSITY

BY

DEFNE ECEM GÜR

IN PARTIAL FULFILLMENT OF THE REQUIREMENTS
FOR
THE DEGREE OF MASTER OF SCIENCE
IN
METALLURGICAL AND MATERIALS ENGINEERING

JANUARY 2025

Approval of the thesis:

SYNTHESIS OF HOLLOW HYDROXYAPATITE PARTICLES FOR ORHOPEDIC APPLICATIONS

submitted by **DEFNE ECEM GÜR** in partial fulfillment of the requirements for the degree of **Master of Science** i**n Metallurgical and Materials Engineering, Middle East Technical University** by,

Prof. Dr. Naci Emre Altun
Dean, **Graduate School of Natural and Applied Sciences**

Prof. Dr. Ali Kalkanlı
Head of the Department, **Metallurgical and Materials Eng.**

Assoc. Prof. Dr. Batur Ercan
Supervisor, **Metallurgical and Materials Eng., METU**

Examining Committee Members:

Prof. Dr. Abdullah Öztürk
Metallurgical and Materials Eng., METU

Assoc. Prof. Dr. Batur Ercan
Metallurgical and Materials Eng., METU

Prof. Dr. Dilek S. Keskin
Engineering Sciences, METU

Prof. Dr. Eda Ayşe Aksoy
Faculty of Pharmacy, Hacettepe Uni.

Assist. Prof. Dr. Şeniz Uçar
Metallurgical and Materials Eng., METU

Date: 10.01.2025

I hereby declare that all information in this document has been obtained and presented in accordance with academic rules and ethical conduct. I also declare that, as required by these rules and conduct, I have fully cited and referenced all material and results that are not original to this work.

Name Last name : Defne Ecem Gür

Signature :

ABSTRACT

SYNTHESIS OF HOLLOW HYDROXYAPATITE PARTICLES FOR ORHOPEDIC APPLICATIONS

Gür, Defne Ecem
Master of Science, Metallurgical and Materials Engineering
Supervisor: Assoc. Prof. Dr. Batur Ercan

January 2025, 48 pages

Hydroxyapatite (HAp, $Ca_{10}(PO_4)_6(OH)_2$), which constitutes 70% of bone tissue, is a bioactive and biocompatible material. Therefore, it is among the most commonly used bone graft materials in bone-tissue engineering. In literature, there are various studies on its use as a potential antibiotic-loaded bone graft to prevent postoperative bone infection (osteomyelitis). Although these studies showed promising results, antibiotic loading capacities were limited with adsorption of the antibiotics onto the HAp particle surfaces. Thus, there is a clear need for bioactive systems that can serve as reservoirs to enhance the antibiotic-loading and prolong its release, while simultaneously inducing bone cell functions for orthopedic applications.

In this thesis, $CaCO_3$ (vaterite) particles were synthesized by a wet precipitation method and used as a template. Subsequently, HAp was precipitated onto the vaterite particles to obtaine Vaterite@HAp (core@shell) structure. To dissolve the vaterite core, acetic acid was used, and hollow HAp structure was obtained.

Hollow HAp particles were loaded with gentamicin, a widely used antibiotic for bone infection. Additionally, these particles were also coated with Rhamnolipid (RL) to prolong the duration of antibiotic release. Antibiotic loaded particles, including Vaterite@HAp particles, hollow HAp particles, and RL coated hollow HAp particles, were evaluated for their antibacterial efficacy against Gram-positive *Staphylococcus aureus (S. aureus)* and Gram-negative *Escherichia coli (E. coli)* strains.

At all investigated time points, gentamicin loaded, RL coated hollow HAp (GRL-HAp) particles exhibited superior antibacterial performance, as evidenced by larger inhibition zone diameters compared to the gentamicin loaded hollow HAp (G-HAp) and gentamicin loaded Vaterite@HAp (G-Vat@HAp) particles. Notably, GRL-HAp particles demonstrated up to 32-fold higher bactericidal activity against *S. aureus*, and more than 4000-fold greater bactericidal activity against *E. coli*.

Furthermore, Cellular viability results demonstrated that HAp, RL-HAp, G-HAp, and GRL-HAp particles were not cytotoxic at 0.1 and 0.01 mg/mL concentrations, and there was no significant difference between groups and TCPS. These results highlight that GRL-Hap particles are promising towards bone infection.

Keywords: Bioceramic, hydroxyapatite, bone graft, particles synthesis.

ÖZ

ORTOPEDİK UYGULAMALAR İÇİN İÇİ BOŞ HİDROKSİAPATİT PARTİKÜL SENTEZİ

Gür, Defne Ecem
Yüksek Lisans, Metalurji ve Malzeme Mühendisliği
Tez Yöneticisi: Doç. Dr. Batur Ercan

Ocak 2025, 48 sayfa

Hidroksiapatit (HAp, $Ca_{10}(PO_4)_6(OH)_2$), kemik dokusunun %70'ini oluşturan biyouyumlu ve biyoaktif bir malzemedir. Bu nedenle, kemik-doku mühendisliği alanında en yaygın kullanılan kemik grefti malzemeleri arasında yer almaktadır. Literatürde, HAp'ın ameliyat sonrası kemik enfeksiyonlarını (osteomiyelit) önlemek amacıyla potansiyel bir antibiyotik yüklü kemik grefti olarak kullanımına yönelik çeşitli çalışmalar bulunmaktadır. Bu çalışmalar umut verici sonuçlar ortaya koysa da antibiyotik yükleme kapasiteleri, antibiyotiklerin HAp partiküllerinin yüzeyine adsorpsiyonu ile sınırlı kalmıştır. Bu nedenle, hem antibiyotik yükleme kapasitesini artıran hem de salınım süresini uzatarak kemik hücre fonksiyonlarını teşvik eden biyoaktif sistemlere duyulan ihtiyaç açıktır.

Bu tez çalışmasında, $CaCO_3$ (vaterit) partikülleri yaş çöktürme yöntemiyle sentezlenmiş ve şablon olarak kullanılmıştır. Daha sonra, vaterit partikülleri üzerine HAp çöktürülerek vaterit@HAp (çekirdek@kabuk) yapısı elde edilmiştir. Vaterit çekirdeğin çözünmesini sağlamak amacıyla asetik asit kullanılmış ve içi boş HAp partikülleri sentezlenmiştir.

Elde edilen içi boş HAp partikülleri, kemik enfeksiyonlarının tedavisinde yaygın olarak kullanılan gentamisin antibiyotiği ile yüklenmiştir. Ayrıca, antibiyotik salınım süresini uzatmak amacıyla bu partiküller rhamnolipid (RL) ile kaplanmıştır. Antibiyotik yüklü partiküller (Vaterit@HAp partikülleri, içi boş HAp partikülleri ve RL kaplı içi boş HAp partikülleri), Gram-pozitif *Staphylococcus aureus* (*S. aureus*) ve Gram-negatif *Escherichia coli* (*E. coli*) suşlarına karşı antibakteriyel etkinlik açısından değerlendirilmiştir.

İncelenen tüm zaman noktalarında, gentamisin yüklü RL kaplı içi boş HAp (GRL-HAp) partikülleri, gentamisin yüklü içi boş HAp (G-HAp) ve gentamisin yüklü Vaterit@HAp (G-Vat@HAp) partiküllerine kıyasla daha geniş inhibisyon alanı oluşturarak üstün antibakteriyel performans sergilemiştir. Özellikle, GRL-HAp partikülleri *S. aureus* karşısında 32 kat, *E. coli* karşısında ise 4000 kat daha yüksek bakterisidal aktivite göstermiştir.

Buna ek olarak, hücresel canlılık sonuçları, HAp, RL-HAp, G-HAp ve GRL-HAp partiküllerinin 0.1 ve 0.01 mg/mL konsantrasyonlarında sitotoksik olmadığını ve gruplar ile TCPS arasında anlamlı bir fark bulunmadığını göstermiştir. Elde edilen sonuçlar, GRL-HAp partiküllerinin kemik enfeksiyonlarının tedavisi açısından umut vadettiğini ortaya koymaktadır.

Anahtar Kelimeler: Biyoseramik, hidroksiapatit, kemik grefti, parçacık sentezi

To my beloved family and grandparents…

ACKNOWLEDGMENTS

First and foremost, I would like to express my deepest gratitude to my advisor, Assoc. Prof. Dr. Batur Ercan, for his invaluable guidance, continuous support, and encouragement throughout my research. His insights, expertise and belief in me at every stage have been instrumental in shaping this work.

I would also like to extend my heartfelt appreciation to Dr. Dilek Türkoğlu for her unwavering support and for bringing positivity into my life. Her guidance has profoundly influenced my perspective and made this journey more meaningful.

I would like to thank technical assistances of our department; Nilüfer Özel for her help in XRD characterization. My sincere thanks also go to Yiğithan Tufan for FTIR measurements.

I am immensely grateful to my dear friends at the Biomaterials and Nanomedicine Laboratory for their collaboration, insightful discussions, and the supportive research environment they have provided. I would like to thank Çağan Olgu Özonuk for his assistance with cellular viability tests and Gülsün Eylül Şengül for her help in particle synthesis. Their contributions have been invaluable to this work.

My deepest gratitude goes to my family for their unconditional love, endless patience, and unwavering encouragement. Their constant support has been my greatest motivation. I am also especially thankful to my grandparents, whose wisdom and kindness have always been a source of inspiration.

Finally, I would like to acknowledge all those who have contributed to this work, directly or indirectly. This journey would not have been possible without their support.

TABLE OF CONTENTS

CHAPTERS

LIST OF FIGURES

FIGURES

LIST OF ABBREVIATIONS

ABBREVIATIONS

HAp: Hydroxyapatite, $Ca_{10}(PO_4)_6(OH)_2$

Core@shell: Vaterite core@Hydroxyapatite shell,

RL: Rhamnolipid

G-Vat@HAp: Gentamicin loaded Vaterite@HAp

G-HAp: Gentamicin loaded HAp

RL-HAp: Rhamnolipid coated HAp

GRL-HAp: Gentamicin loaded and rhamnolipid coated HAp

PBS: Phosphate-Buffered Saline

SEM: Scanning Electron Microscopy

TEM: Transmission Electron Microscopy

HR: High Resolution

SAED: Selected Area Diffraction

XRD: X- ray Diffraction

FTIR: Fourier Transform Infrared Spectroscopy

ATR: Attenuated Total Reflection

TGA: Thermogravimetric Analysis

DTA: Differential Thermal Analysis

BET: Brunauer-Emmet-Teller

BJH: Barret-Joyner-Halenda

IUPAC: International Union of Pure and Applied Chemistry

OD: Optical Density

CFU: Colony Forming Unit

S. aureus: Staphylococcus aureus

E. coli: *Escherichia coli*

TSB: Tryptic soy broth

LIST OF SYMBOLS

SYMBOLS

^{o}: degree

~: approximate

CHAPTER 1

INTRODUCTION

Bone damage resulting from trauma, age-related bone resorption, and tumor-induced bone loss has been treated with bone grafts in orthopedic surgery for many years [1,2,3]. Bone grafting provides an osteoconductive and/or osteoinductive environment that promotes bone healing and regeneration [4,5]. Bone healing process initiates with osteoinduction, which involves the differentiation of pluripotent stem cells into osteoblasts. Proliferation and formation of new bone tissue are supported by osteoconductive properties of bone grafts [1,6,7,8]. Clinically, one of the mostly used bone graft material is hydroxyapatite (HAp, $Ca_{10}(PO_4)_6(OH)_2$). 70% of bone tissue and 98% of tooth enamel consist of HAp, which is a bioactive, biocompatible, and bioresorbable material [1]. It can be sourced from animal bones, plants or aquatic sources (Figure 1.1), and chemically synthesized [7,8]. Notably, chemically synthesized HAp exhibits comparable tissue compatibility to its naturally sourced counterpart [1]. HAp is recognized as the most commonly utilized bioceramic in bone tissue engineering [2,6,9]. It has been shown that HAp positively affected the adhesion and proliferation of osteoblast cells (bone cells) [10]. Through these advantageous properties, HAp serves as an effective carrier for antibiotic loading, enabling sustained antimicrobial activity and reducing the risk of post-surgical infections in orthopedic applications.

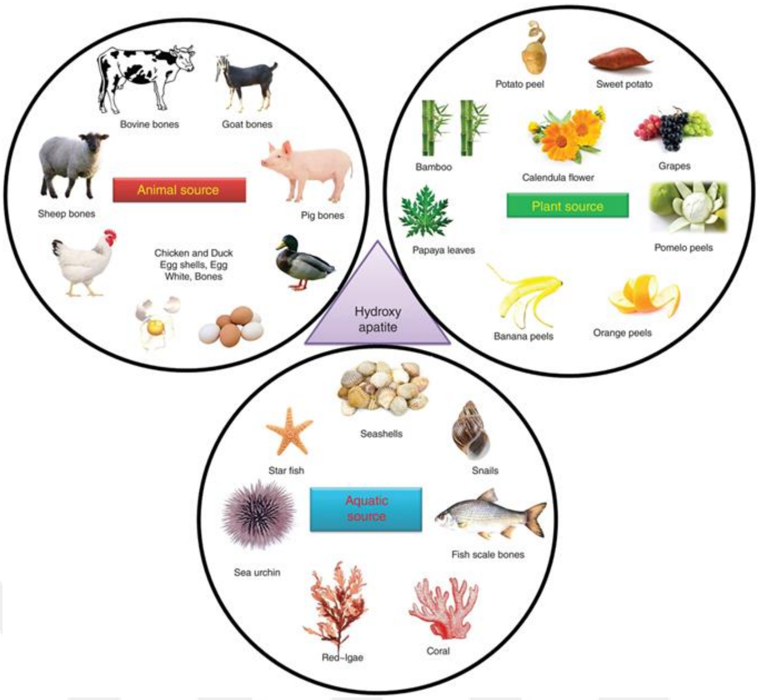

Figure 1.1 Natural sources of HAp: Animal-derived, plant-based resources, and aquatic origins [8].

1.1 Gentamicin

Gentamicin is an aminoglycoside antibiotic consisting of three sugar rings and several amino groups. Under physiological conditions (pH ~7.4), its amino groups become protonated and form $-NH_3^+$ groups. These protonated amino groups were shown to interact with the negatively charged phosphate groups of the bacterial 30S ribosomal subunit, thereby inhibiting protein synthesis [11]. Gentamicin is a broad-spectrum antibiotic, exhibiting bactericidal activity against both Gram-negative and Gram-positive bacteria. Additionally, it is characterized by its low molecular weight, cost-effectiveness, and widespread availability. Due to its broad-spectrum efficacy, gentamicin is commonly used for the treatment of bone infections [12,13]

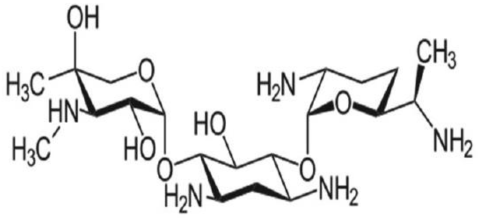

Figure 1.2 Chemical formula of Gentamicin [14].

1.2 Rhamnolipid

Rhamnolipid (RL) is a glycolipid type of biosurfactant, derived from Gram-Negative *Pseudomonas aeruginosa* bacteria [15]. RL contains both hydrophobic and hydrophilic groups which are polar rhamnose units (one or two) and non-polar fatty acid chain [16,17]. These amphipathic structures enhance the antibacterial activity of RL, which is well-known for its anti-adhesive and anti-biofilm characteristics [18,19].

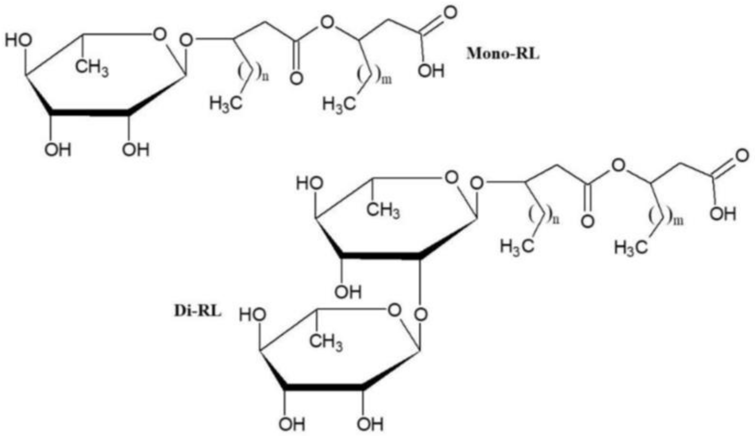

Figure 1.3 Molecular formula of mono- and di-rhamnolipids [20].

1.3 Research Objective

This research aimed to synthesize hollow and mesoporous HAp particles that can serve as reservoirs to enhance the antibiotic-loading capacity, while simultaneously inducing bone cell functions for orthopedic applications. Hollow and mesoporous structure had high surface area and porosity, which are essential for maximizing drug encapsulation and facilitating controlled release.

The primary aim of this study was to synthesize hollow and mesoporous hydroxyapatite (HAp) particles to serve as reservoirs, thereby enhancing antibiotic-loading capacity while simultaneously promoting bone cell functions for orthopedic applications.

HAp particles were synthesized using the anion exchange method. Following synthesis, the HAp particles were loaded with gentamicin, a potent aminoglycoside antibiotic, to effectively target and mitigate bone infections. To further optimize the antibiotic release profile, the gentamicin-loaded hollow HAp particles were subsequently coated with rhamnolipid (RL). This coating is critical for maintaining therapeutic antibiotic concentrations over an extended period, thereby improving infection management and reducing the risk of antibiotic resistance.

CHAPTER 2

LITERATURE REVIEW

2.1 Hollow Hydroxyapatite (HAp) as Antibiotic Loaded Bone Graft

In orthopedic surgeries such as the fixation of open bone fractures and joint revision surgeries, various factors such as the operative environment, the attire worn by medical personnel, and microorganisms inherently present on the patient's skin, serve as primary sources of bacterial contamination. Gram-positive *Staphylococcus aureus (S. aureus)* and Gram-negative *Escherichia coli* (*E. coli*) are primarily responsible for approximately 90% of postoperative bone infections observed in patients [21,22,23,24]. Following primary bone surgery, oral or intravenous antibiotic therapy is administered to prevent infections caused by these opportunistic bacteria [8]. However, achieving therapeutic concentrations of antibiotics within bone tissue is challenging due to its limited vascularization [6]. Therefore, opportunistic bacteria in the surgical area adhere to bone tissue and/or implant surfaces, followed by formation of biofilm which is a self-produced polysaccharide-based extracellular matrix. When bacteria form biofilm, the antibiotic concentrations required to eradicate it gets 10 to 100-fold higher than the applied systemic antibiotic concentrations [21]. The residual bacteria in the area may even develop resistance to suboptimal antibiotic levels. Over time, bone infection will develop and lead to failure of the primary surgery [25]. This makes the treatment of osteomyelitis more complicated and often necessitates a second surgical intervention [23]. Secondary operations typically involve comprehensive debridement (wound cleaning), removal of necrotic tissue, and the replacement of the implant [26].

To mitigate the risk of bone infection following orthopedic procedures, recent studies have focused on local antibiotic therapy [6,27,28]. This approach aims to deliver antibiotics at therapeutic concentrations directly to the bone tissue without being affected by poor vascularity and preventing the antibiotic toxicity in healthy tissues. There are studies on the use of HAp as a potential antibiotic-loaded bone graft to prevent postoperative osteomyelitis [29,30]. The aim of these studies is to achieve a sustained and prolonged release of the loaded antibiotics.

Antibiotic loading potential and antibiotic release kinetics of HAp particles depend on various parameters that can be controlled through the synthesis method and procedure of HAp [31,32,33]. While antibiotic release kinetics depend on pore size and degradation rate of HAp, antibiotic loading potential is influenced by particle size, shape, surface area, pore volume, and structure of HAp particles. One study reported that the release kinetics of gentamicin from HAp particles increased with larger pore size. Conversely, the amount of gentamicin loading decreased as the porosity of the particles decreased [32].

Similarly, HAp particles with a large surface area and mesoporous structure (Figure 2.1a, b) exhibited an antibiotic-loading capacity up to three times higher than conventional HAp. While the antibiotic release of mesoporous HAp particles reached a plateau in 5 days, the antibiotic release of conventional HAp particles was completed within the first 6 hours (Figure 2.1c).

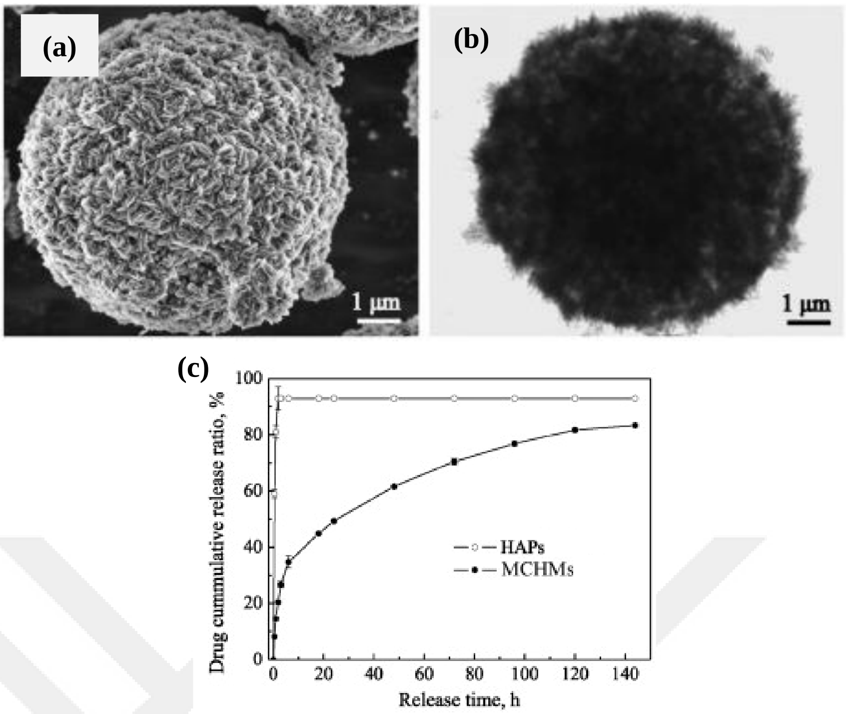

Figure 2.1 (a) SEM and (b) TEM bright field image of mesoporous carbonated hydroxyapatite microspheres (MCHMs). (c) Cumulative drug release of MCHMs and hydroxyapatite (HAPs) [34].

Additionally, as the concentration of gentamicin loaded onto these particles increased, the number of bacteria on the surfaces decreased, with no observed toxic effects on stromal cells [34].

In another study, the antibiotic-carrying performance of HAp particles and the release kinetics of surface-bound antibiotics were tested, and the results showed that the antibiotic was released rapidly, completing within a short period of about 30 minutes [35].

Jiang et al. implanted powdered vancomycin and HAp particles in tablet form into animals as artificial bone to improve bone tissue loss resulting from chronic osteomyelitis. The results indicated that the antibiotic-loaded artificial bone was gradually resorbed and replaced by new bone tissue, while infection did not recur in the damaged tissue [36].

Although these studies focused on antibiotic release from HAp particles, studies on the effects of antibiotic-loaded HAp on bone cell functions and antibacterial activity remained limited and insufficient. Moreover, in these studies, antibiotics in powder form were either directly mixed with HAp-based bone grafts or the grafts were soaked in prepared antibiotic solutions. Therefore, antibiotics were adsorbed only onto the outer surface of the HAp particles.

However, such methods led to rapid release of the antibiotic, resulting in rapid release and compromised efficacy for the local antibiotic therapy. Thus, there is a need to synthesize particles that can act as reservoirs, allowing for prolonged and increased antibiotic release. To enhance the drug-loading capacity of HAp, only a few studies have reported synthesizing it in a shell form with a hollow core. In these studies, HAp was loaded with anti-cancer and anti-inflammatory drugs, and time-dependent drug release was analyzed via absorbance methods.

In a study conducted by Lai et al., hollow HAp particles (Figure 2.2a) were synthesized using an anion exchange method followed by a hydrothermal process. These particles were loaded with the anti-cancer drug doxorubicin hydrochloride (DOX), and it was observed that DOX release from the particles was completed within 96 hours (Figure 2.2b). The DOX-loaded particles exhibited selective cytotoxicity: effectively killing hepatocarcinoma cells (Figure 2.3a), showing reduced toxicity to healthy hepatocytes (Figure 2.3b) [30].

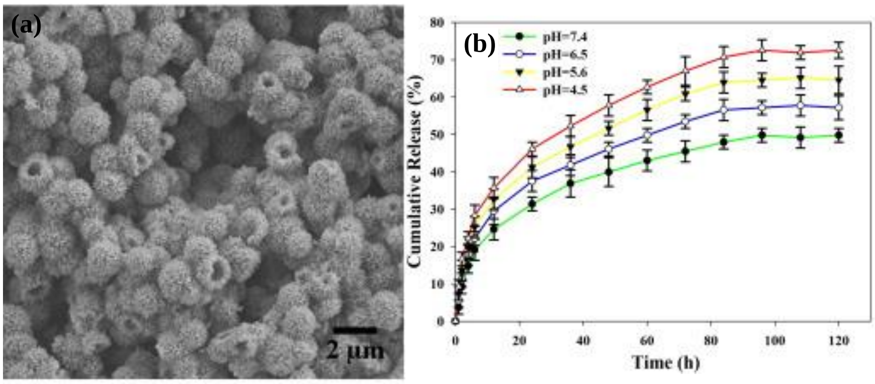

Figure 2.2 (a) SEM image of the porous hollow HAp microspheres and (b) DOX release profiles of the particles in PBS [30].

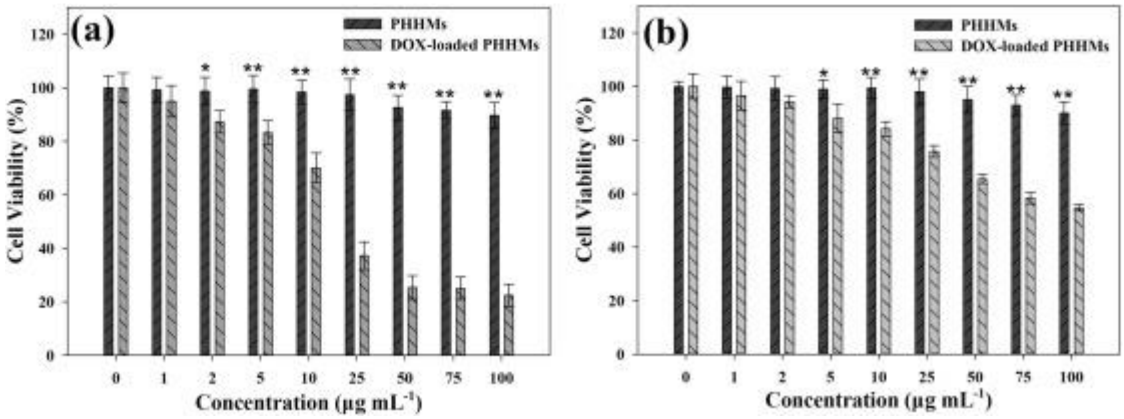

Figure 2.3 (a) Cellular viability of the particles with and without DOX using human hepatocarcinoma cells and (b) human hepatocyte cells [30].

Another research group synthesized hollow HAp particles (Figure 2.4a) using the wet precipitation and hydrothermal methods and loaded them with doxorubicin (DOX). Drug release from the particles reached a plateau within 20 hours (Figure 2.4b) [37]. To investigate the cytotoxicity of DOX-loaded HAp, CCK-8 viability assays were performed using MC3T3-E1 cells, and it was observed that the number of viable cells increased with the culture period.

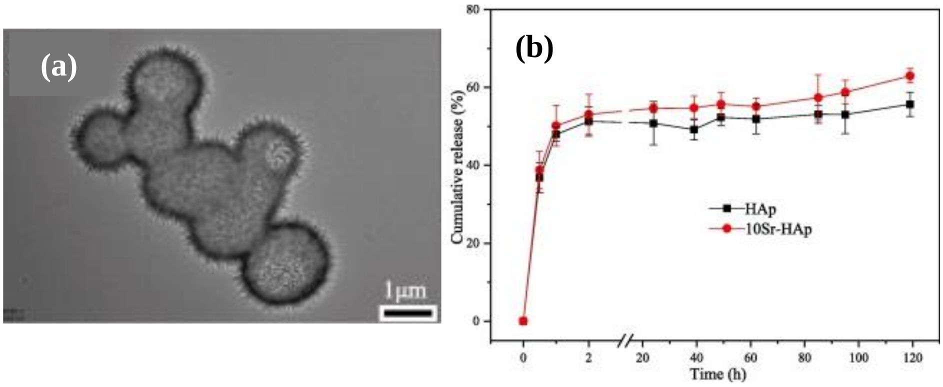

Figure 2.4 (a) TEM images of HAp hollow microspheres and (b) Cumulative DOX release of particles in PBS at pH 7.4 [37].

In another study, hollow HAp particles were loaded with the anti-inflammatory drug ibuprofen. The ibuprofen-loaded HAp was compressed into disk form. Release kinetics of particles were compared to pure ibuprofen disk. While the release of pure ibuprofen was completed within 2.5 hours (Figure 2.5a), the release of ibuprofen from the HAp disks reached a plateau after 48 hours (Figure 2.5b). However, this study did not assess cellular interaction or antibacterial activity [38].

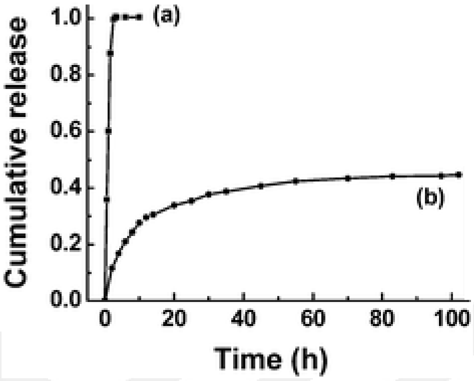

Figure 2.5 (a) Release of a pure ibuprofen disk, and (b) ibuprofen-loaded HAp disk in SBF [38].

In a study by Safi et al., an attempt was made to synthesize cubic-shaped hollow HAp particles via an anion exchange method and loaded them with ibuprofen [39]. However, cubic morphology was not preserved during synthesis of hollow particles, which led to ruptured structures. Consequently, the drug release was completed in a short period of 4 hours.

As stated previously, none of the studies in literature involved loading antibacterial drugs into the HAp shells or testing their performance with bacterial cells. There is only one study that synthesizes hollow HAp and loads antibiotics into the particles.

In this study, a $CaCO_3$ core was synthesized, and a HAp shell was precipitated onto it using an anion exchange method. Subsequently, the $CaCO_3$ core was dissolved with the aid of acetic acid to obtain a hollow HAp shell. However, during synthesis, the particles fused together, lost their morphology, and resulted in ruptured particle structures. To test the release kinetics of ciprofloxacin from the particles, the antibiotic-loaded particles were placed in a dialysis membrane, followed by immersing them in phosphate-buffered saline (PBS) solution. The absorbance of this solution was measured at specific time intervals. It was observed that approximately 50% of the loaded drug was released over 9 days. However, at these specific release time points, fresh PBS was not added to the particles in place of the collected release solution. As a result, this method is inadequate for accurately determining the potential duration of antibiotic release from the particles [40].

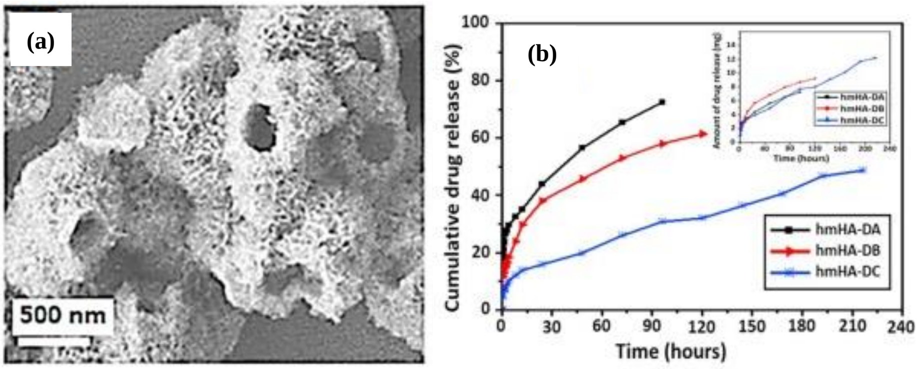

Figure 2.6 (a) SEM images of hollow mesoporous HAp particles (hmHANPs) (b) ciprofloxacin release of hmHANPs at pH 7.4 [40].

Although the aforementioned studies demonstrated that the drug loading capacity of the hollow particles was increased, it was observed that the drug release durations were shorter than anticipated. Moreover, no measures, such as coating the particles, were taken to prolong antibiotic release. HAp particles loaded with drugs could be coated with lipid-based materials to achieve the desired drug release kinetics [41,42].

Rhamnolipid (RL), derived from Pseudomonas aeruginosa and known for its anti-adhesive and anti-biofilm properties [18,19], is a candidate lipid for coating HAp-based materials. For example, RL-coated poly (lactic-co-glycolic acid) (PLGA) nanoparticles were found to have prolonged release of doxorubicin/erlotinib compared to those without the RL coating [43].

Currently, there is no available system for orthopedic applications that can both regulate the release of antibiotics from a reservoir and induce bone healing simultaneously.

The aim of this thesis was synthesis of hollow and porous HAp particles and load them with antibiotic, gentamicin, selected for its broad-spectrum activity, to combat infections in bone tissue. To prolong the antibiotic release kinetics, the particle surfaces were coated with RL. The antibacterial efficacy of the synthesized particles was tested against Gram-positive *S. aureus* and Gram-negative *E. coli* to fight against bone infection.

CHAPTER 3

EXPERIMENTAL METHODS

3.1 Materials

All the chemicals used in this study were analytical grade. Calcium acetate monohydrate (Ca $(CH_3CO_2)_2H_2O$), sodium bicarbonate ($NaHCO_3$), ethylene glycol (EG; $(CH_2OH)_2$), phosphoric acid (H_3PO_4, ≥ 85 wt%) and ethanol (C_2H_5OH) and were purchased from Sigma Aldrich and Millipore Milli-Q purification system was used to obtain ultrapure water. Minimum Essential Medium α (MEM-α) and fetal bovine serum (FBS) were purchased from Serena. 3-(4,5-Dimethylthiazol-2-yl)-2,5-Diphenyltetrazolium bromide (MTT) kit was purchased from Abcam. Dimethyl sulfoxide (DMSO), and hexamethyldisilazane (HMDS) were purchased from Sigma Aldrich. Gentamycin sulphate, rhamnolipid (RL) and tryptic soy broth (TSB) were purchased from Biobasic, Agae Technologies, and Merck, respectively.

3.2 Synthesis of Vaterite@HAp and Hollow HAp Particles

Ellipsoidal vaterite ($CaCO_3$) particles were initially synthesized as template particles using a wet precipitation method. For the synthesis of vaterite particles, calcium acetate monohydrate (0.3 M) and sodium bicarbonate (0.9 M) solutions were prepared. EG was added to each solution, and the solutions were stirred at 500 rpm for 4 min. Subsequently, the calcium acetate monohydrate and sodium bicarbonate solutions were mixed, and stirred at 500 rpm for 15 min. The mixture was then left to stand for 1 h to facilitate vaterite particle precipitation. Afterwards, the vaterite particles were sequentially washed with ethanol and distilled water. To form a HAp shell on the vaterite cores (Vaterite core@HAp shell), diluted phosphoric acid solution prepared in EG was added to the particles. To dissolve the vaterite core and form a hollow HAp shell, the Vaterite@Hap (Vat@HAp, core@shell) structure was treated with diluted acetic acid solution. Finally, the particles were rinsed with ethanol and distilled water.

3.3 Antibiotic Loading and Lipid Coating of the Particles

To facilitate antibiotic loading, Vat@HAp (40 mg) and HAp (40 mg) particles were immersed in 10 mL of a 4 mg/mL gentamicin sulfate solution prepared in 1X PBS for 4 hours, after which they were referred to as G-Vat@HAp and G-HAp, respectively. After loading, the particles were centrifuged and rinsed with distilled water to remove unbound antibiotics. For lipid coating of the particles, RL solution was used. Initially, RL was dissolved in 1X PBS at a 1:1 mass ratio with the particles. Subsequently, HAp and G-HAp particles were immersed in the RL solution for 2 h to allow coating, followed by collection of particles via centrifugation and washing with distilled water. After RL coating particles were referred to as RL-HAp and GRL-HAp, respectively

3.4 Characterization of particles

3.4.1 Scanning Electron Microscopy (SEM)

The surface morphology of the particles was examined using a Scanning Electron Microscope (SEM) (FEI Nova Nano SEM 430). Before SEM imaging, particles were coated with a thin layer of gold using a Quorum SC7640 sputter coater to prevent electrical charge accumulation. SEM imaging was taken under 20kv of accelerating voltage.

3.4.2 Transmission Electron Microscopy (TEM)

Transmission Electron Microscopy (TEM, FEI TECHNAI F30) was employed at 200 kV accelerating voltage to visualize the hollow structure of the particles and obtain crystallographic data under bright-field and high-resolution (HR) modes. Particle size and shell thickness were measured from these images using ImageJ software.

3.4.3 X-ray diffraction (XRD)

X-ray diffraction (XRD) was utilized to confirm the crystal structure of the particles. For this purpose, measurements were conducted using a Brucker D8 Advance X-ray diffractometer) with monochromatic Cu Kα radiation (λ = 1.54 Å) at a scan rate of 2°/min over a 2θ range of 20°-60°.

3.4.4 Fourier Transform Infrared Spectroscopy (FTIR)

The chemical characterization of the particles was performed using Fourier Transform Infrared Spectroscopy (FTIR, Perkin Elmer 400) in attenuated total reflection (ATR) configuration. Samples were scanned in the range of 4000-400 cm^{-1} with 4 cm^{-1} resolution.

3.4.5 Thermogravimetric Analysis (TGA)

The particles were subjected to Thermogravimetric Analysis (TGA) and Differential Thermal Analysis (DTA) using a Perkin Elmer Pyris 1 TGA system. For thermal characterization, the particles were heated in a nitrogen atmosphere at a rate of 10°C/min from T_{room} to 950 °C.

3.4.6 Brunauer-Emmett-Teller (BET)

The surface area (m^2/g), pore size distribution, and pore volume of the particles were characterized using a Brunauer-Emmett-Teller (BET) surface characterization device (Quantachrome Corporation, Autosorb-6). Prior to BET characterization, particles were degassed at 70 °C for 5 h. N_2 adsorption-desorption isotherms were presented, along with the corresponding pore size distribution. The results were characterized according to the International Union of Pure and Applied Chemistry (IUPAC) classification. Surface area, pore size and distribution and pore volume of the particles were calculated based on the Barret-Joyner-Halenda (BJH) model.

3.5 *In vitro* Antibiotic release

The antibiotic-loaded particles, including G-Vat@HAp, G-HAp, and GRL-HAp, were immersed in fresh 1X PBS with a pH of 7.4 to study antibiotic release. At specific time intervals (1, 6, 12, 24 h, and 3, 5, 7, 9, 11, 13, 15, 19, 21, 23, 25, 27, 29 days) the particles were centrifuged, and all release media were collected for analysis. At the end of each interval, particles were immersed in fresh 1X PBS.

3.6 Antibacterial properties

To assess the antibacterial properties of the particles, inhibition zone (disk diffusion) and colony forming unit (CFU) assays were performed with Gram-positive *Staphylococcus aureus* (ATCC 25923) and Gram-negative *Escherichia coli* (ATCC 10536) strains. Standard bacterial culture protocols were followed. Initially, for both inhibition zone and CFU experiments, bacteria were inoculated onto tryptic soy agar (TSA) for 24 h. Following inoculation, a single colony was transferred to tryptic soy broth (TSB) and cultured in a shaking incubator at 37°C with agitation at 200 rpm for 4 h. After incubation, the optical density (OD) of the cultures was measured at a wavelength of 600 nm, and the bacterial suspensions were diluted to achieve an OD of 0.1. This OD corresponds to approximately 1.5 × 10^8 colony-forming units (CFU)/mL, as determined using the 0.5 McFarland scale [44].

For the inhibition zone experiment, 0.5 mL of the prepared bacteria suspensions were spread onto TSA plates. Sterile cellulose filters were placed onto bacteria-spread agar plates, and 10 µL of the release liquids, collected at different time intervals (up to 29 days) from antibiotic loaded particles (G-Vat@HAp, G-HAp, and GRL-HAp) were added onto the filters. After incubation at 37°C for 24h, inhibition zones were measured.

For the CFU experiments, bacteria suspensions were diluted to achieve a concentration of 10^6 CFU/mL using TSB for both bacteria strains. These bacteria suspensions were then mixed with release liquids (1: 100 diluted) in equal volumes. After incubation at 37°C for 24 h, the media in the wells were serially diluted and plated onto agar. Number of CFUs were counted after an incubation period of 24 h.

3.7 Bone Cell Viability

Prior to the *in vitro* biological tests, particles were sterilized with 70% ethanol solution for 15 min, followed by exposing to UV radiation for 1 h. MC3T3-E1 pre-osteoblast cells (ATCC CRL-2593) were cultured using Minimum Essential Medium α (MEM-α) supplemented with 10% FBS, 1% L-glutamine, and 1% penicillin/streptomycin. The cells were cultured under standard cell culture conditions (37°C and 5% CO_2). For viability tests, sterilized particles were extracted in cell culture medium at concentrations of 0.1 and 0.01 mg/ mL at 37°C for 72 h. MC3T3-E1 cells were seeded into 96-well plates at a density of 10,000 cells/well and incubated for 24 h under standard conditions (37°C and 5% CO_2) to allow for attachment of the cells. After 24 h, the culture media were replaced with extract solutions. The metabolic activities of the cells were assessed for up to 5 days using the MTT kit. At the specified time points, the media were aspirated, and the cells were rinsed with 1X PBS. 1 mg/mL MTT solutions were added to wells, and incubated for 4 h (37°C, 5% CO_2). After 4 h, an isopropanol solution containing 0.1 M HCl was added to wells to dissolve the formazan crystals. Subsequently, absorbance values were read at a wavelength of 560 nm using a microplate absorbance reader (Thermo Scientific Multiskan GO). The obtained values were normalized by subtracting the absorbance values of control samples without cells. Using a standard absorbance-cell count graph, total cell counts were determined.

3.8 Statistical analysis

All biological experiments were conducted in triplicate, with four samples used for each repetition. The results were presented as mean ± standard deviation. Statistical analyses were performed using Tukey's post hoc test, with the significance level set at $p<0.05$.

CHAPTER 4

GENTAMICIN LOADED HOLLOW HAP PARTICLES

4.1 Results and Discussion

Initially, vaterite (Figure 4.1a) particles in ellipsoidal morphology were synthesized as template. Then, HAp shells were precipitated on the vaterite ($CaCO_3$) core (vaterite core@HAp shell) (Figure 4.1b). During the HAp shell precipitation onto vaterite cores, ellipsoidal shape of particles was maintained and the change in surface morphology was observed in the SEM image (Figure 4.1b). For the synthesis of hollow HAp particles**,** the vaterite core was dissolved by using 1:65 diluted acetic acid solution for 3.5 minutes. After acetic acid treatment, hollow shell structured particles (Figure 4.1c) were successfully obtained preserving the ellipsoidal morphology without rupture of the particles. Hollow structure of HAp seen in bright field imaging in TEM characterization (Figure 4.3a).

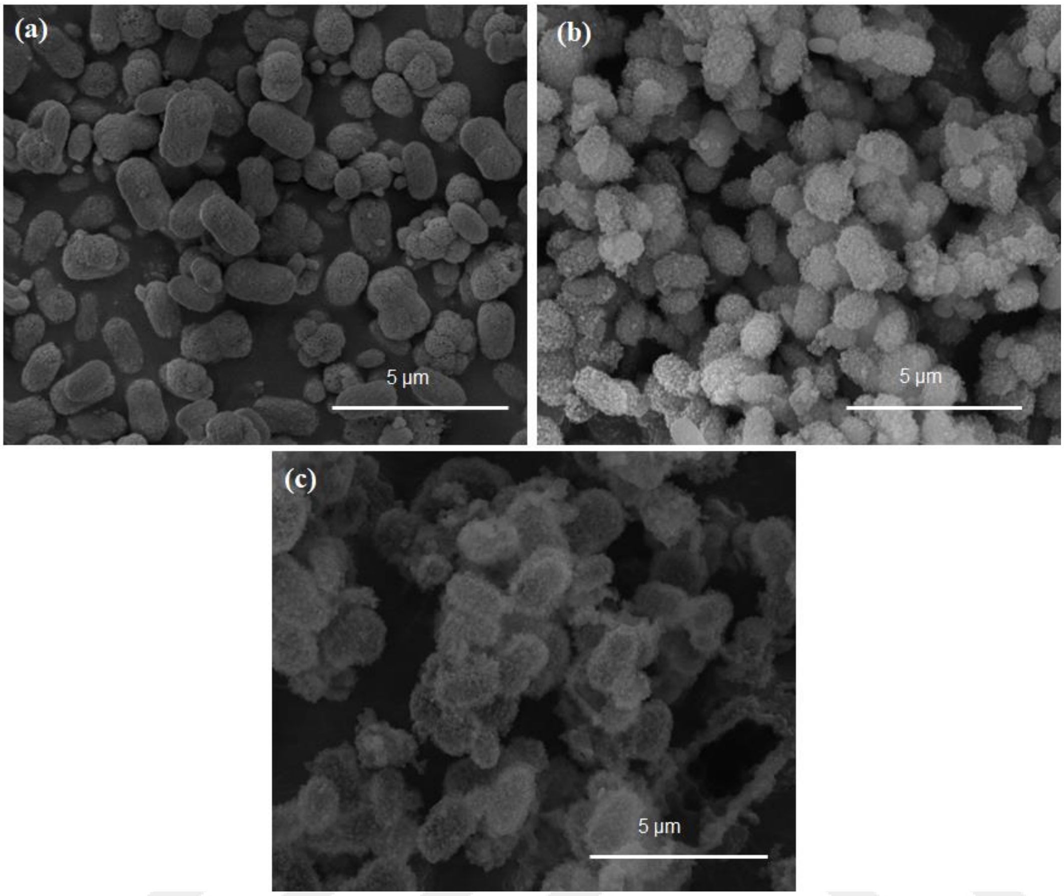

Figure 4.1 SEM images of (a) Vaterite ($CaCO_3$), (b) Vat@ HAp, and (c) HAp particles.

XRD analysis was used for phase identification of the synthesized particles (Figure 4.2). XRD pattern of $CaCO_3$ particles (blue line) provided peaks at 21.06, 24.99, 27.16, 32.88, 38.93, 42.76, 43.95, 49.19, 50.13, 55.88 which belonged to (004), (110), (112), (114), (211), (008), (300), (304), (118) and (224) crystal planes respectively. According to JCPDS references $CaCO_3$ core was vaterite (#033–0268) polymorph. The emergence of HAp phase peaks in the diffraction pattern is evidence of HAp precipitation onto the vaterite core (red line). XRD analysis was performed to confirm the totally dissolution of the vaterite (#009–0432) core upon acid treatment to remain hydroxyapatite (#009–0432) shell structure. Diffraction peaks of the HAp particles (black line) are 22.85, 25.82, 31.97, 39.83, 46.58, 49.50, 53.15

corresponding to (111), (002), (211), (310), (222), (213), and (004) crystal planes respectively. Broad diffraction peaks of HAp indicate the semicrystalline structure of HAp shells. During antibiotic loading and RL coating processes, there were no phase transformations of HAp were observed (Figure 4.2, green line).

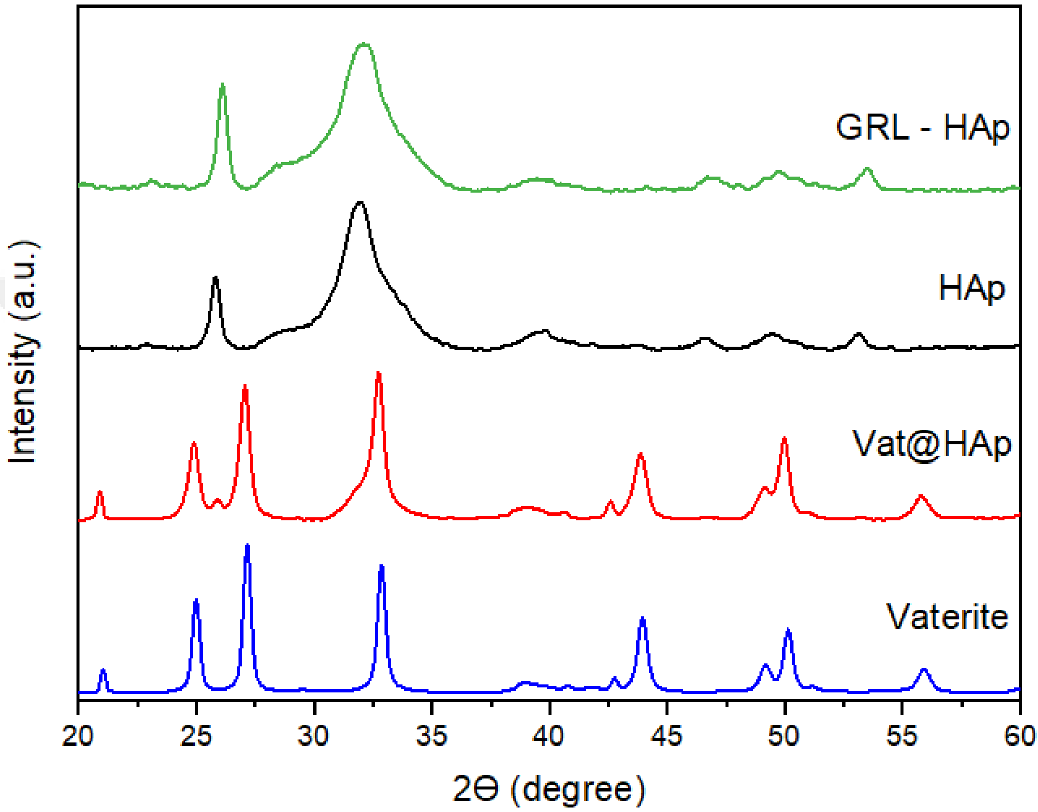

Figure 4.2 XRD spectra of the synthesized particles.

TEM characterization was conducted for HAp and RL-HAp particles (Figure 4.3) to confirm the hollow structure of particles and coating. Selected Area Electron Diffraction (SAED) patterns of the HAp particles (Figure 4.3b) exhibited diffusive and distinct rings, indicating that the particles possess a semicrystalline structure. These findings are consistent with the corresponding XRD spectra (Figure 4.2, black line). In bright field TEM imaging of RL-HAp particles (Figure 4.3c), RL coating was not observed.

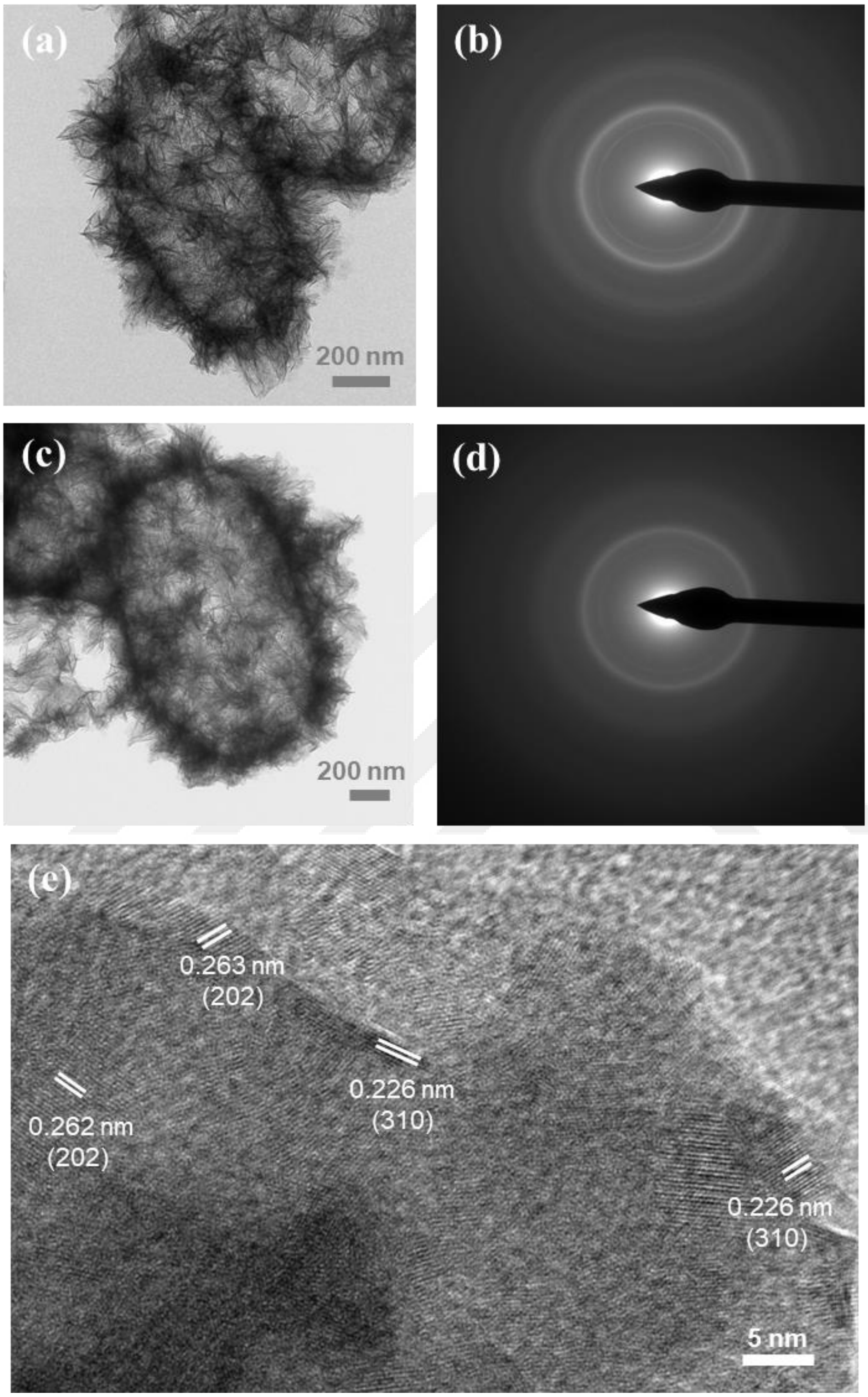

Figure 4.3 (a and c) Bright field TEM images of a) HAp, and c) RL-HAp particles, (b and d) SAED patterns of b) HAp, and d) RL-HAp particles, and e) HR-TEM image of HAp particles.

In the FTIR spectra (Figure 4.4)**,** characteristics absorption bands of the CO_3^{2-} in the vaterite particles (blue line) are 745 cm^{-1} (out-of-plane bending vibration), 849 cm^{-1} (bending vibration), 876 cm^{-1} (bending vibration) and 1089 cm^{-1} (symmetric stretching vibration) [45,46,47,48]. For the HAp particles (black line), the bands appearing at 478 cm^{-1} (bending vibration), 561 cm^{-1} (out-of-plane bending vibration), 601 cm^{-1} (out-of-plane bending vibration) 960 cm^{-1} (symmetric stretching vibration), 1020 cm^{-1} (asymmetric stretching vibration) and 1120 cm^{-1} (asymmetric stretching vibration) belong to the characteristics PO_4^{3-} absorptions bands. The absence of characteristic vaterite absorption bands for HAp particles in the FTIR spectra indicates that the vaterite core is fully dissolved and removed [49]. Furthermore, absorption bands at 875 cm^{-1} (bending vibration) and 1411 cm^{-1} (asymmetric stretching vibration) belong to B-type CO_3^{2-} substitution in HAp phase for the PO_4^{3-} ions which is the evidence of carbonated HAp [50,51,52]. CO_3^{2-} substitution caused deviation from stoichiometric HAp composition. While it did not alter the phase of HAp and its X-ray diffraction pattern (Figure 4.2), it will alter the crystallinity and cause the broadening of diffraction peaks. It should be noted that HAp phase in natural bone is also non-stoichiometric, nanocrystalline and carbonate substituted [7,53]. Under physiological conditions, nonstoichiometric HAp is more resorbable and has a higher osteoconductive property than stoichiometric HAp [9,54,55,56]. Due to CO_3^{2-} ion substitution for the PO_4^{3-} ions, hydroxyl bands at 630 cm^{-1} (libration) and 3500 cm^{-1} (stretching) in HAp particles are absent [57,58]. This is resulting in the removal of an OH^- ion from the structure to balance the charge difference. After synthesis of HAp particles, they were loaded with gentamicin to serve as reservoirs for local antibiotic delivery, as detailed in section 3.3 followed by coating with RL to prolonged antibiotic release and to enhance antibacterial properties.

The loading of gentamicin into the HAp particles is confirmed by the presence of characteristic primary amine (bending, $-NH_2$), secondary amine (deformation, -NH) and secondary amine (bending, -NH) bands at 1644 cm^{-1}, 1551 cm^{-1} and 1467 cm^{-1} respectively [59,60,61,62,63]. Moreover, the RL coating of the HAp particles were confirmed by the identification of intense bands at 2958 cm^{-1} (asymmetric stretching $-CH_3$), 2925 cm^{-1} (asymmetric stretching $-CH_2$), 2854 cm^{-1} (symmetric stretching $-CH_2$), 1735 cm^{-1} (symmetric stretching, $-C=O$) and 1401 cm^{-1} (symmetric stretching, $-COO^-$) [17,60,61,64,65].

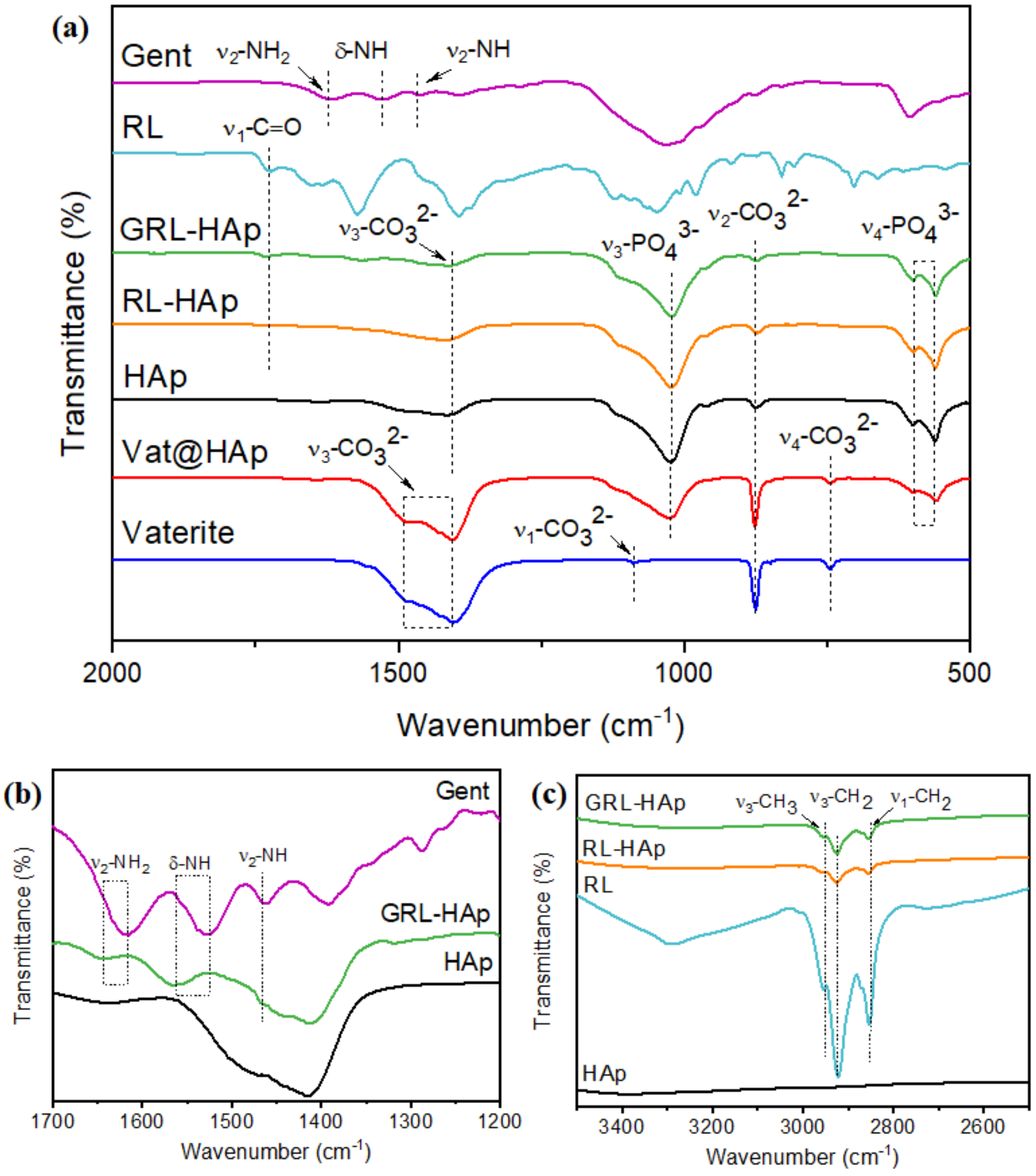

Figure 4.4 FTIR spectra of the synthesized particles between a) 2000-500 cm^{-1}, b) 1700-1200 cm^{-1}, and c) 3500-2500 cm^{-1}.

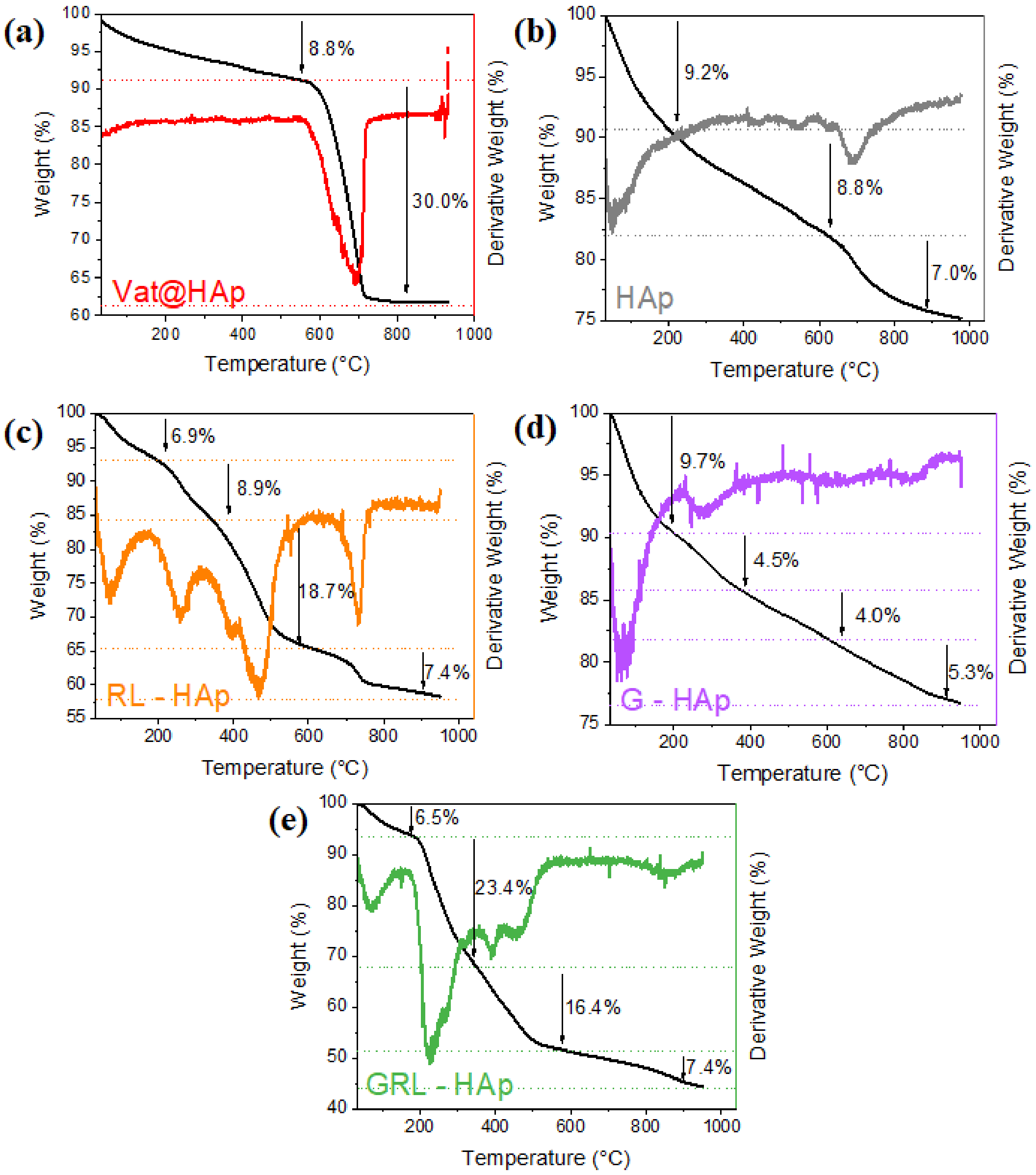

Figure 4.5 TGA and DTG curve of a) Vat@HAp, b) HAp, c) RL-HAp, d) G-HAp, and e) GRL-HAp particles.

The TGA and DTG curves of particles (Figure 4.5) illustrate the weight loss and thermal behavior of particles upon heating from T_{room} to 975°C.

For Vat@HAp particles (Figure 4.5a), 7% weight loss is observed up to 400 °C, attributed to the physically bonded and structural water. Decomposition of carbonate content occurs between 600°C and 800°C, with the maximum decomposition rate observed at 690°C.

HAp (Figure 4.5b), RL-HAp (Figure 4.5c), G-HAp (Figure 4.5d) and GRL-HAp particles (Figure 4.5e) exhibit weight losses of 9.2%, 6.9%, 9.7% and 6.5%, respectively, up to 200°C due to physically bonded water.

Between 600°C and 800°C, weight losses of 7.0%, 7.4%, 5.3%, and 7.4% are observed, respectively, due to the carbonate decomposition of these particles (Figure 4.5b, c, d, and e). RL-HAp particles (Figure 4.5c) exhibit a 27.6% weight loss between 200°C and 600°C. The decomposition of rhamnose groups in rhamnolipid occurs at 260°C, with the maximum decomposition rate, followed by the decomposition of the hydrocarbon chain at 396°C and 473°C, at their respective maximum rates. G-HAp particles (Figure 4.5d) exhibit 4.5% weight loss between 200°C and 400°C. The decomposition of gentamicin's amine and hydroxyl groups have the maximum decomposition rate at 276°C. GRL-HAp particles (Figure 4.5e) show 39.8% total weight loss between 200°C and 600°C, primarily due to the decomposition of gentamicin with maximum decomposition rates at 228°C, and decomposition of rhamnolipid with maximum decomposition rates at 270°C and 392°C.

While antibiotic release kinetics have been shown to depend on the pore size and degradation rate of HAp, antibiotic loading potential was influenced by factors such as the particle size, shape, surface area, pore volume [31,32,33]. To assess the surface properties of the particles, Brunauer-Emmett-Teller (BET) surface characterization was applied. BET analysis revealed the surface area (m^2/g), pore size distribution, and pore volume of the particles. Vat@HAp, HAp and RL-HAp particles have Type V adsorption-desorption isotherms. According to the International Union of Pure and Applied Chemistry (IUPAC) classification, Type V isotherms are characterized by relatively weak adsorbent-adsorbate interactions at low p/p_0 values. At higher p/p_0 values, type V isotherms indicate multilayer adsorption, followed by pore filling which is the evidence of mesoporous nature of particles. The Type H3 hysteresis loop was observed in the isotherms of all particles. The H3 hysteresis loop indicates that the particles are agglomerated and possess slit-shaped pores with a broad range of pore size distribution. The Barrett, Joyner, and Halenda (BJH) method was applied to calculate the surface area (m²/g), mesopore size (nm), and pore volume (cc/g) of particles through the analysis of N_2 adsorption–desorption isotherms. HAp has the highest surface area (306.2 m²/g), followed by Vat@HAp (188.9 m²/g) and RL-HAp with the lowest surface area (152.2 m²/g). In mesopore volume measurements, HAp has higher mesopore volume (0.96 cm³/g) than the RL-HAp (0.47 cm³/g) and Vat@HAp and (0.47 cm³/g). In addition, the average pore size of HAp (3.39 nm) was higher than RL-HAp (1.65 nm).

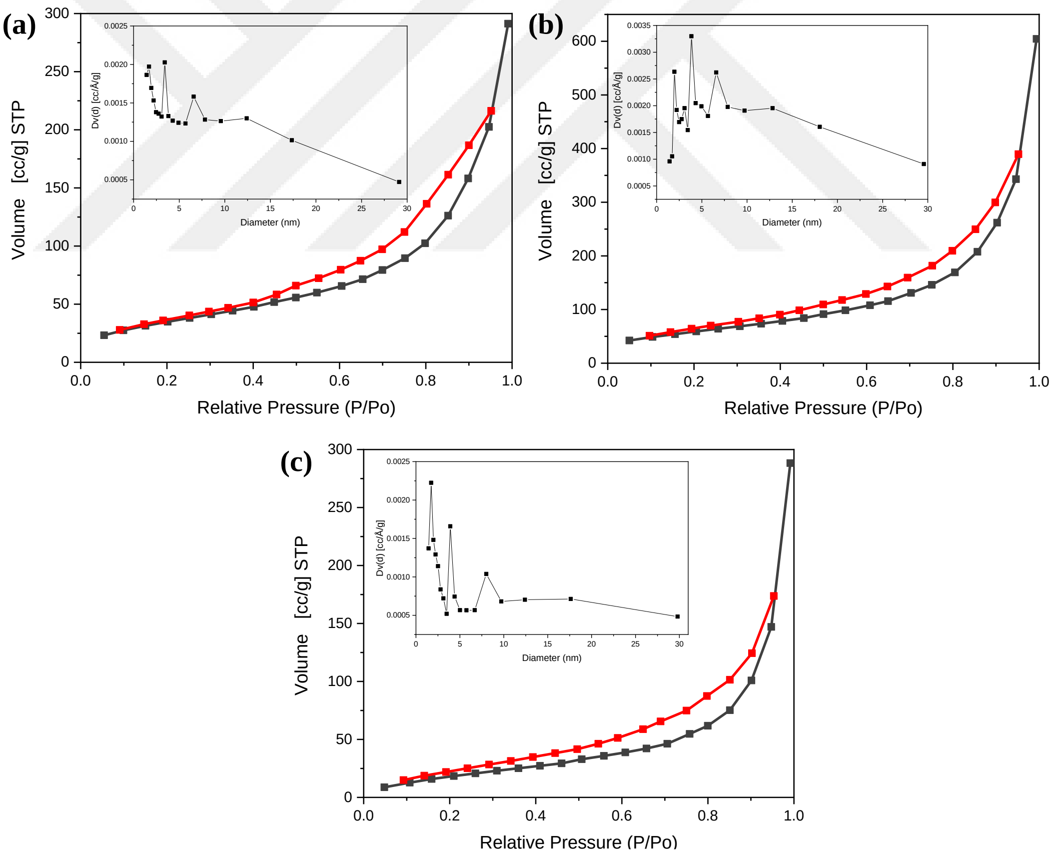

Figure 4.6 Adsorption and desorption curves, and pore size distributions of a) Vat@HAp b) HAp, and c) RL-HAp.

4.2 Antibacterial Performance

Antibacterial performance of antibiotic loaded particles, including G-Vaterite@HAp, G-HAp, and GRL-HAp was tested against *S. aureus* and *E. coli* strains. Following incubation at 37°C for 24 hours, inhibition zones for *S. aureus* (Figure 4.7) were observed on TSA plates using release liquids collected at different time points. While the inhibition zones of G-Vat@HAp particles visible up to 15 days, the inhibition zones of G-HAp and GRL-HAp particles seen up to 29 days.

At all-time points, G-HAp particles exhibited the larger inhibition zone areas compared to G-Vat@HAp particles. This superior performance can be attributed to differences in antibiotic loading mechanisms. While antibiotic molecules only adsorbed onto the outer surface of Vat@HAp particles, HAp particles allow for both internal loading and surface adsorption of antibiotic. The drug loading capacity is significantly enhanced by synthesizing the particles as hollow, facilitating the efficient loading of gentamicin through electrostatic interactions between the negatively charged HAp particles and the positively charged gentamicin molecules. Furthermore, for all time points, gentamicin GRL-HAp particles have larger inhibition zone areas compared to G-HAp particles. This enhancement is attributed to the negatively charged RL, which strengthens the electrostatic attraction of positively charged gentamicin, thereby increasing the drug loading capacity.

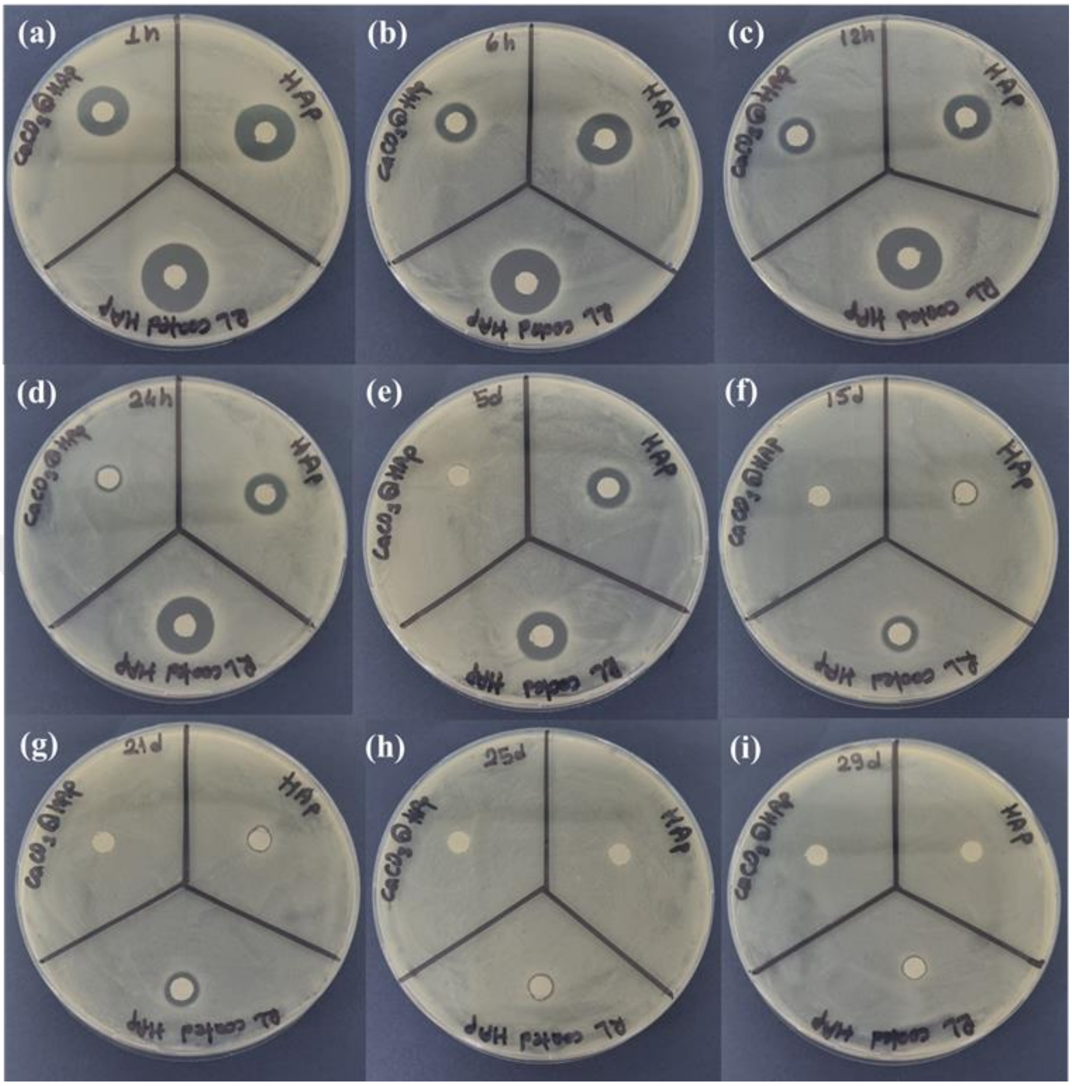

Figure 4.7 Inhibition zones of G-Vat@HAp (left), G-HAp (right) and GRL-HAp (bottom) particles on *S. aureus* at 1 h, 6 h, 12 h, 24 h, 5 day, 15 day, 21 day, 25 day and 29 day' time points.

The inhibition zone areas of release liquids were measured by using Image J software and summed up to generate a cumulative inhibition zone area graph as shown in Figure 4.8 for *S. aureus.* Cumulative inhibition zone area of G-Vat@HAp, G-HAp, and GRL-HAp measured as 725, 1470, 2017 mm^2, respectively.

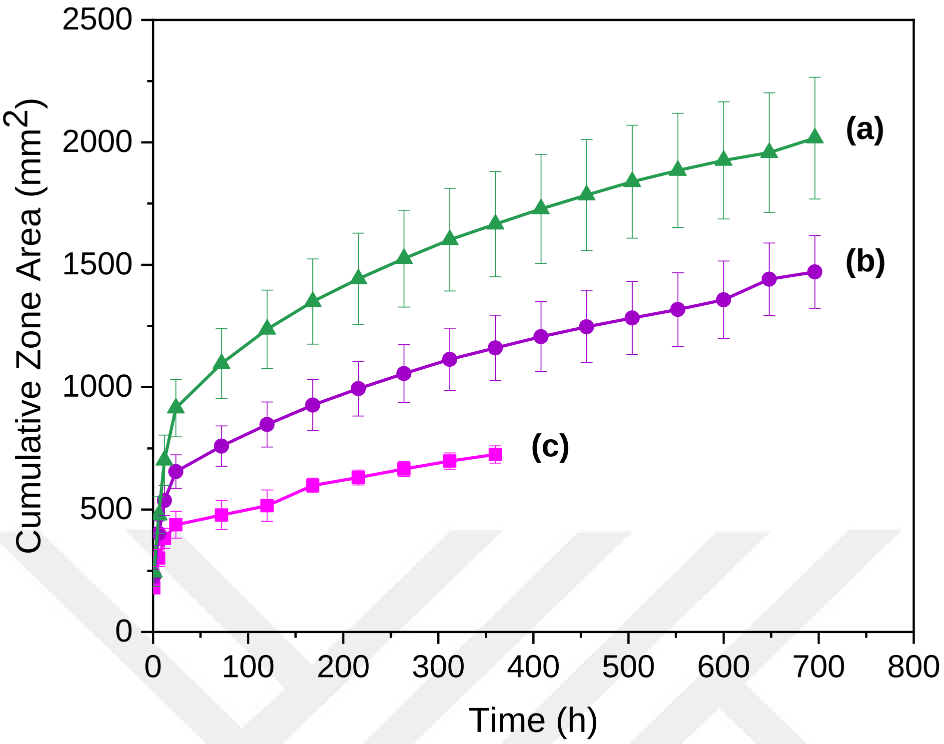

Figure 4.8 Cumulative inhibition zone areas of a) GRL-HAp, b) G-HAp, and c) G-Vat@HAp particles on *S. aureus*. N=3.

Inhibition zones for *E. coli* (Figure 4.9) were observed on TSA plates using release liquids collected at different time points. While the inhibition zones of G-Vat@HAp particles visible up to 24 h, the inhibition zones of G-HAp particles seen until day 13, and GRL-HAp particles seen up to day 21. Cumulative inhibition zone area for *E. coli* (Figure 4.10) of G-Vat@HAp, G-HAp, and GRL-HAp measured as 402, 923, 1437 mm^2, respectively.

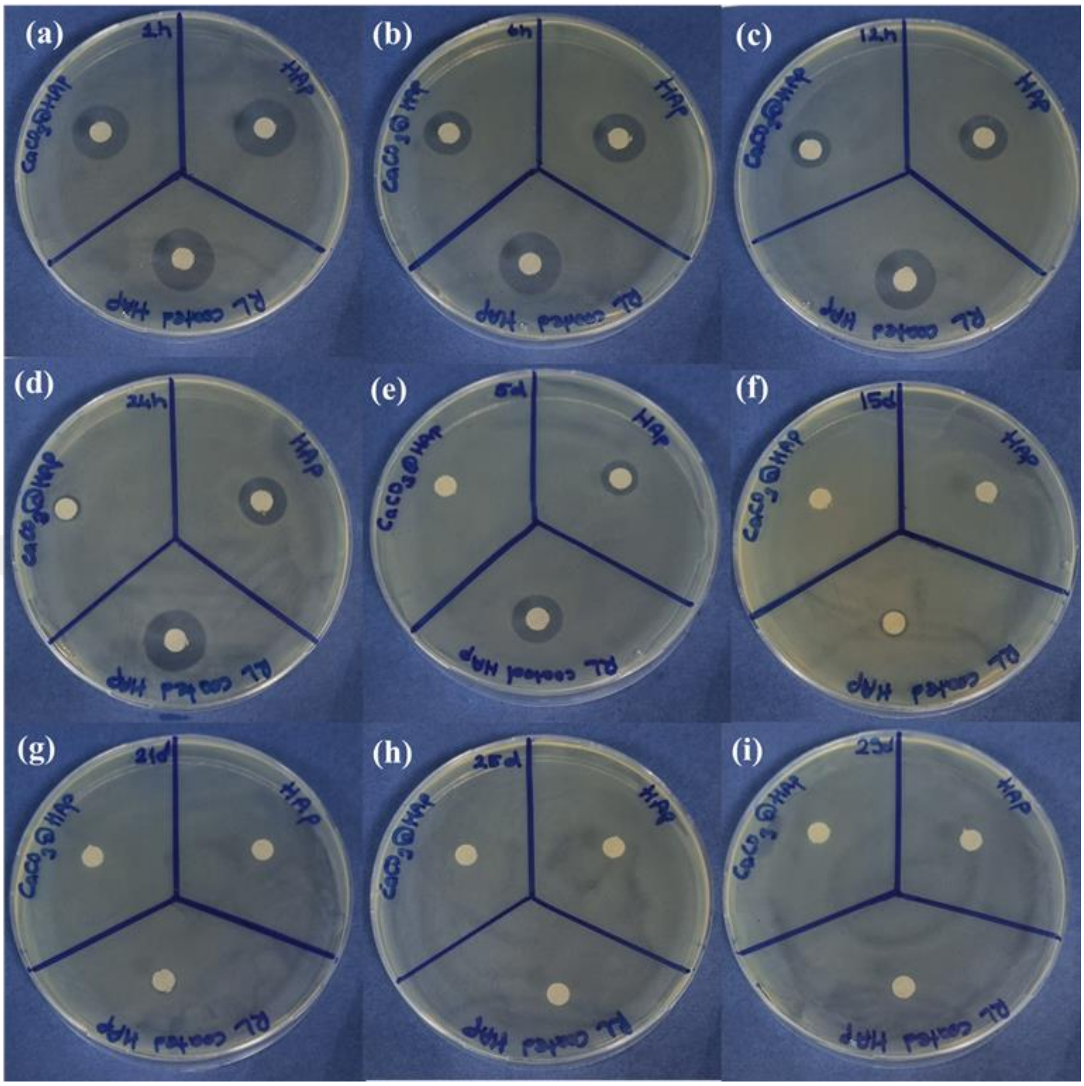

Figure 4.9 Inhibition zones of G-Vat@HAp (left), G-HAp (right) and GRL-HAp (bottom) particles on *E. coli* at 1 h, 6 h, 12 h, 24 h, 5 day, 15 day, 21 day, 25 day and 29 day’ time points.

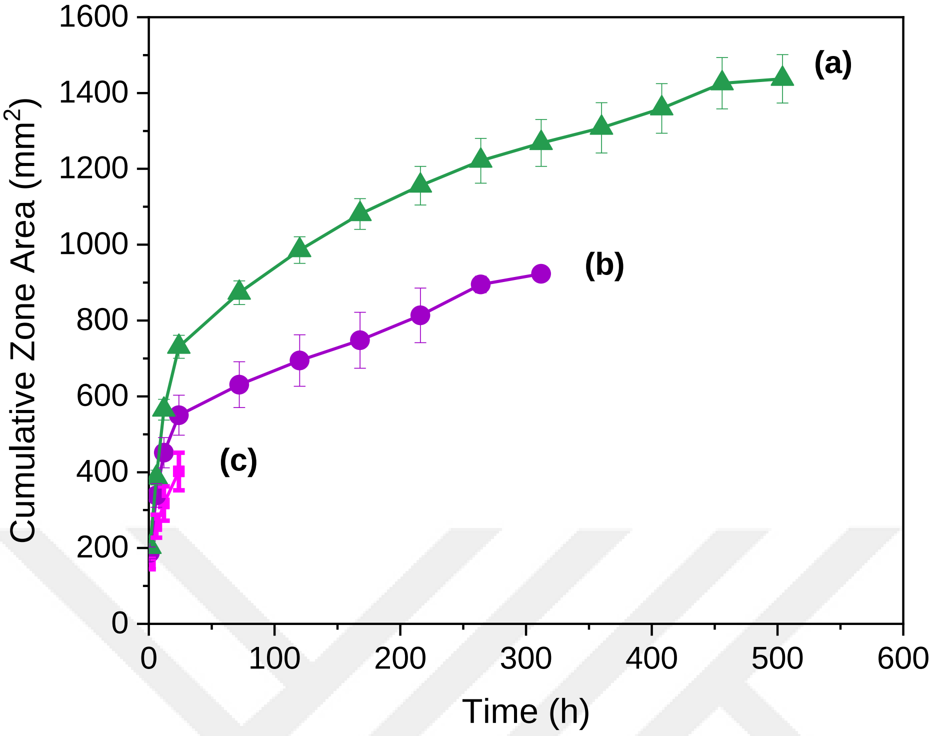

Figure 4.10 Cumulative inhibition zone area of a) GRL-HAp, b) G-HAp, and c) G-Vat@HAp particles on *E. coli*. N=3.

The released liquids collected on day 29 were diluted at a 1:100 ratio, and colony-forming unit (CFU) assays were conducted using these liquids for *S. aureus* and *E. coli* strains.

CFU assay graphs (Figure 4.11) and TSA plate (Figure 4.12) results on *S. aureus* show that there were no significant differences between the G-Vat@HAp, G-HAp, and control (*S. aureus*) groups. However, GRL-HAp particles demonstrated up to a 32-fold greater bactericidal activity against *S. aureus*.

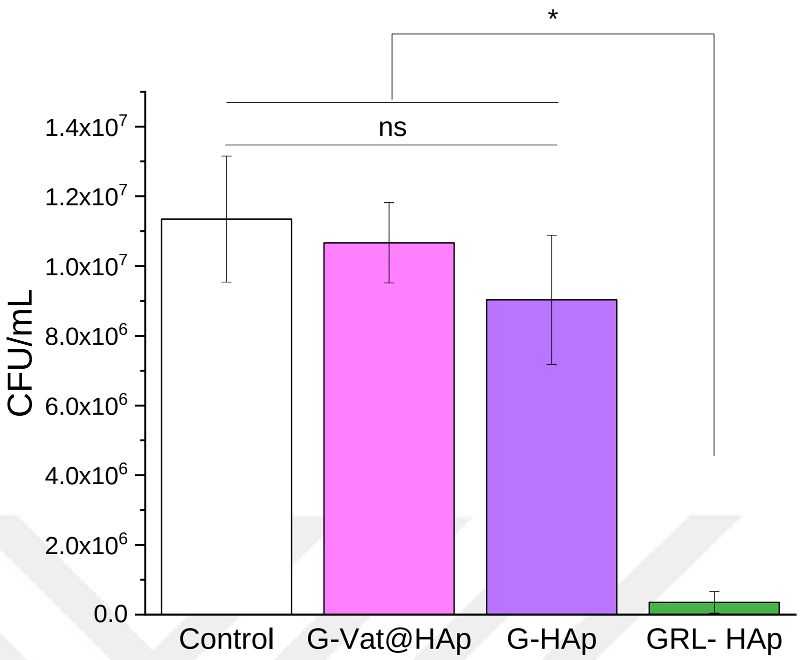

Figure 4.11 *S. aureus* CFUs upon the interaction with 29th day release (includes only 28th and 29th days) of gentamicin from the particles. *p<0.001, N=3.

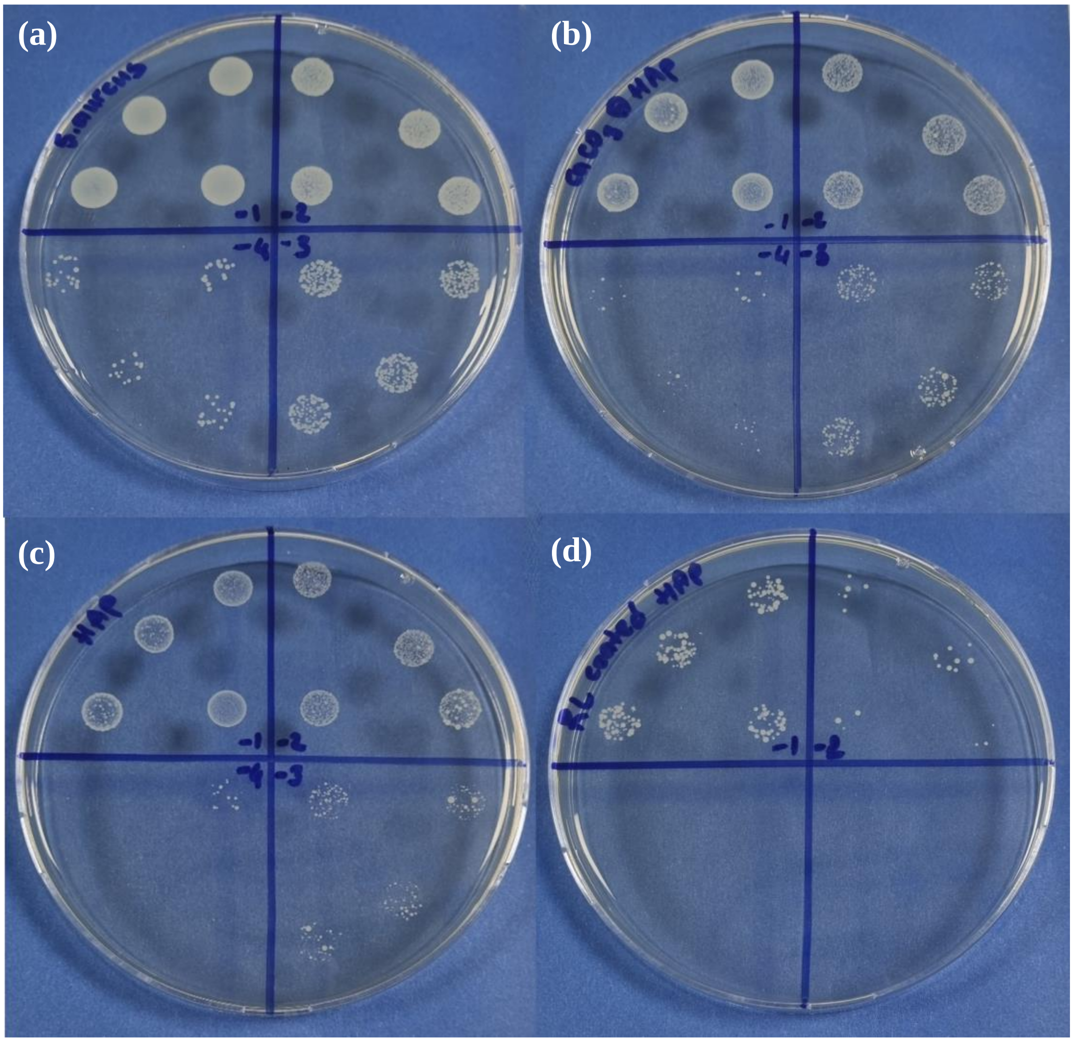

Figure 4.12 Agar plate photographs of *S. aureus* upon the interaction with 29th day release (includes only 28th and 29th days) of gentamicin from a) Control, b) G-Vat@HAp, c) G-HAp, and d) GRL-HAp particles.

CFU assay graphs (Figure 4.13) and TSA plate (Figure 4.14) results on *E. coli* show that there were no significant differences between the G-Vat@HAp, and control (*E. coli*) groups. G-HAp particles reduce the bacteria colony count compared to control group. GRL-HAp particles demonstrated up to a 4623-fold greater bactericidal activity against *E. coli*.

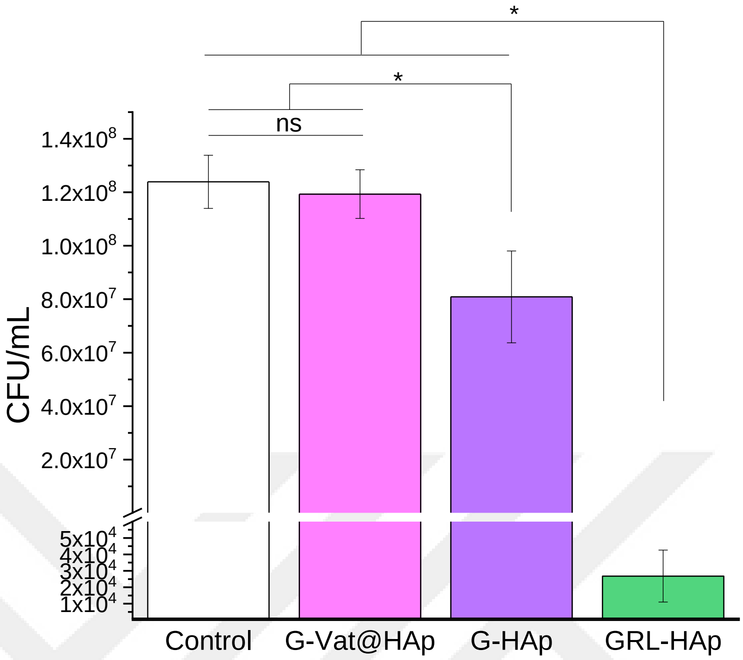

Figure 4.13 *E. coli* CFUs upon the interaction with 29th day release (includes only 28th and 29th days) of gentamicin from the particles. *p<0.001, N=3.

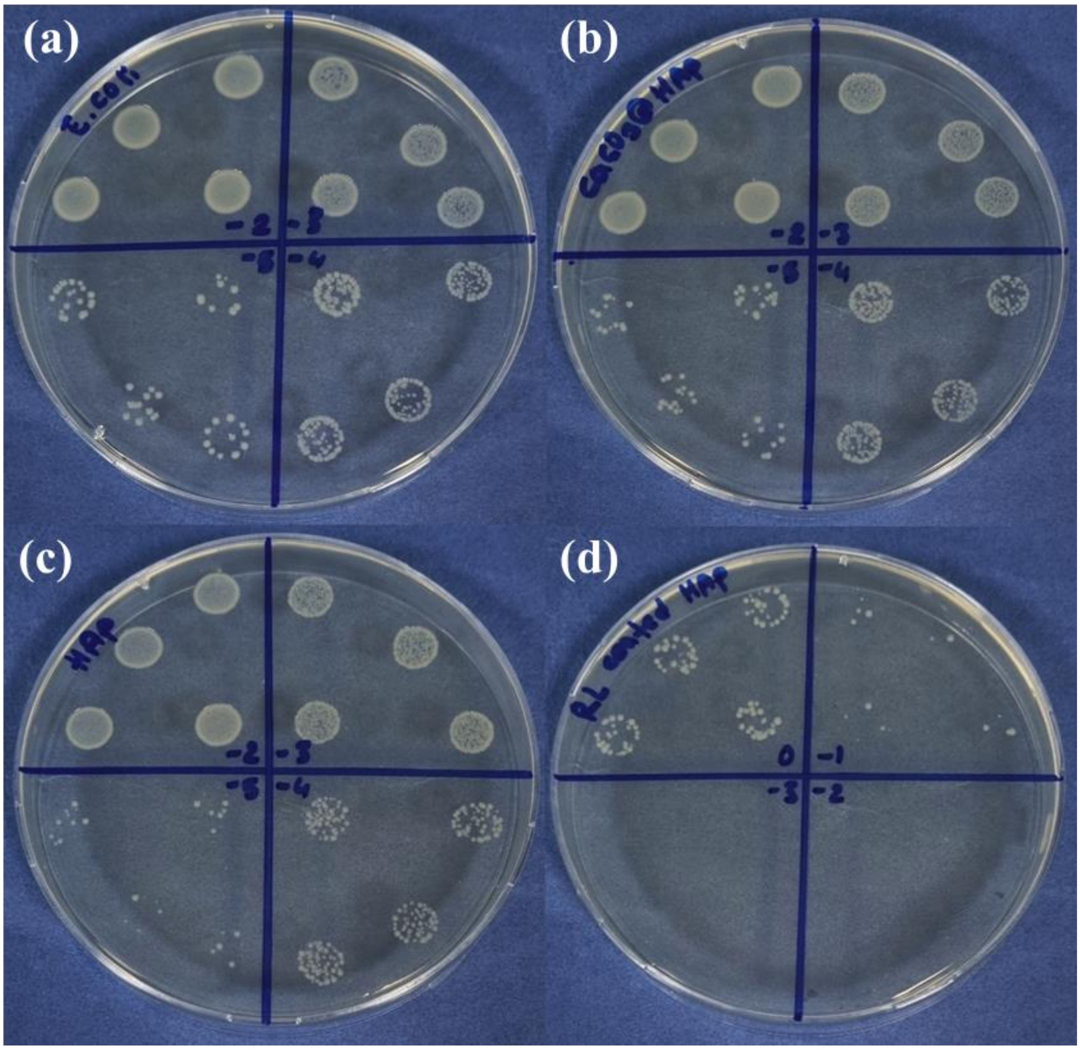

Figure 4.14 Agar plate photographs of *E. coli* upon the interaction with 29th day release (includes only 28th and 29th days) of gentamicin from a) Control, b) G-Vat@HAp, c) G-HAp, and d) GRL-HAp particles.

4.3 Cellular Viability Assay

To assess the cytotoxicity of HAp, RL-HAp, G-HAp and GRL-HAp particles, MTT assay was conducted using the MC3T3-E1 cell line. For the viability experiments, cells were cultured with particle extracts at 0.1 and 0.01 mg/mL concentrations up to 5 days *in vitro*. The control group was tissue culture polystyrene (TCPS). Cellular viability results are provided in Figure 4.15. Results showed that there was no significant difference between any group on the 1st and 3rd days of culture ($p>0.05$). On the 5th day of *in vitro* culture, samples at either extraction concentration did not show any statistical difference compared to the TCPS.

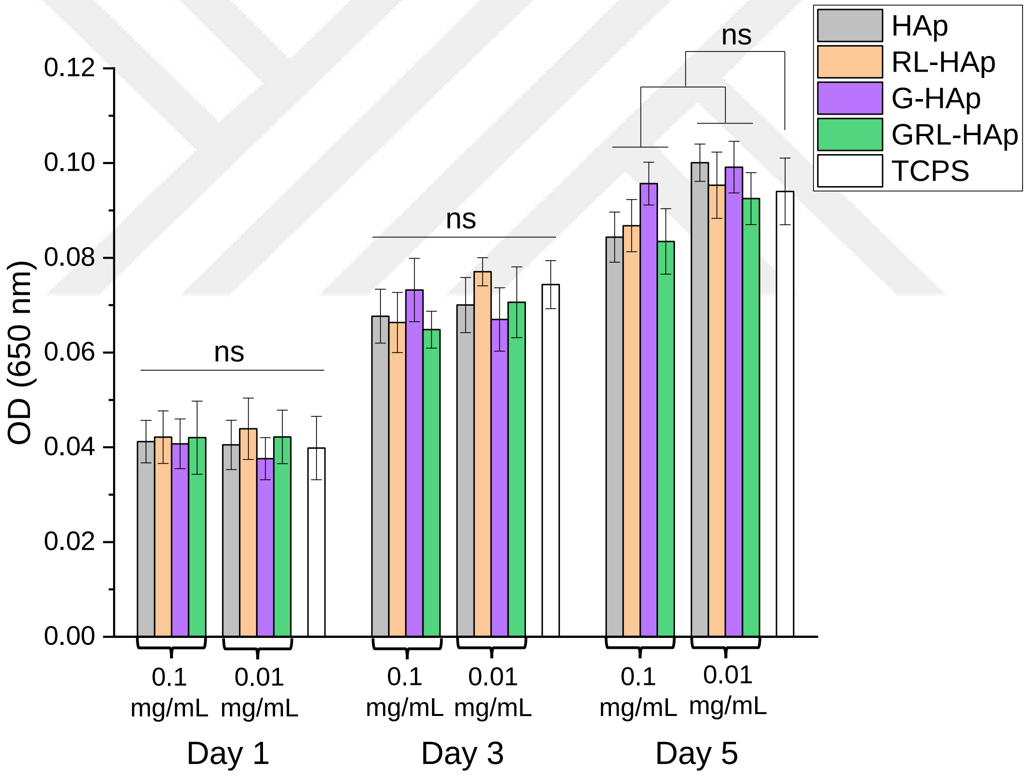

Figure 4.15 Effect of particle extracts (72h, 37 ^{0}C) on MC3T3-E1 (preosteoblast) proliferation. N=3.

CHAPTER 5

CONCLUSION AND FUTURE WORK

5.1 Conclusion

In this thesis, hollow HAp particles were successfully synthesized with the aim of using them as antibiotic-loaded reservoirs to combat bone tissue infection that may occur after bone and orthopedic implant surgeries. Particle characterization studies confirmed that the synthesized particles were carbonated HAp, with no residual vaterite phase. Gentamicin was loaded into the inner core and adsorbed onto the particle surfaces of HAp. To prolong the antibiotic release and sustain the antibacterial coating, the hollow HAp particles were coated with RL.

Surface characterization studies show that HAp had higher surface area (306.2 m^2/g), greater mesopore volume (0.96 cm^3/g) and larger average pore size (3.39 nm) than RL-HAp. This indicates that the RL coating reduced the surface area, mesopore volume, and average pore size of HAp particles. The antibacterial properties of G-Vaterite@HAp, G-HAp, and GRL- HAp particles were evaluated against *S. aureus* and *E. coli* strains using inhibition zone and colony-forming unit (CFU) assays. G-HAp and GRL-HAp particles exhibited inhibition zones against *S. aureus* for up to 29 days, whereas G-Vat@HAp particles exhibited inhibition zones for only 15 days.

At all the time investigated points, GRL-HAp particles showed the largest inhibition zone areas compared to the other particles. The cumulative inhibition zone areas on *S. aureus* were 725, 1470, and 2017 mm^2 for G-Vat@HAp, G-HAp, and GRL-HAp particles, respectively.

For *E. coli*, the inhibition zones of the G-Vat@HAp particles were visible up to 24 hours, G-HAp particles showed inhibition until day 13, and GRL-HAp particles exhibited inhibition up to day 21. The cumulative inhibition zone areas for *E. coli* were 402, 923, and 1437 mm² for the G-Vat@HAp, G-HAp, and GRL-HAp particles, respectively. CFU assay results revealed that GRL-HAp particles demonstrated up to 32-fold higher bactericidal activity against *S. aureus* and more than 4000-fold greater bactericidal activity against *E. coli*.

Furthermore, the cellular viability assay demonstrated that HAp, RL-HAp, G-HAp, and GRL-HAp particles were not cytotoxic at 0.1 and 0.01 mg/mL concentration.

Results indicated that the development of GRL-HAp particles represented a promising approach for improving antibiotic delivery and promoting bone cell viability *in vitro* for bone graft applications.

REFERENCES

1. Dutta SR, Passi D, Singh P, Bhuibhar A. Ceramic and non-ceramic hydroxyapatite as bone graft material: a brief review. Irish Journal of Medical Science (1971 -) 2015; 184: 101–106.

2. Szcześ A, Hołysz L, Chibowski E. Synthesis of hydroxyapatite for biomedical applications. Adv Colloid Interface Sci 2017; 249: 321–330.

3. Föger-Samwald U, Kerschan-Schindl K, Butylina M, Pietschmann P. Age Related Osteoporosis: Targeting Cellular Senescence. International Journal of Molecular Sciences 2022, Vol 23, Page 2701 2022; 23: 2701.

4. Fillingham Y, Jacobs J. Bone grafts and their substitutes. Bone and Joint Journal 2016; 98B: 6–9.

5. Roberts TT, Rosenbaum AJ. Bone grafts, bone substitutes and orthobiologics. Organogenesis 2012; 8: 114–124.

6. Lalidou F, Kolios G, Drosos GI. Bone infections and bone graft substitutes for local antibiotic therapy. Surg Technol Int 2014; 24: 353–362.

7. Eliaz N, Metoki N. Calcium Phosphate Bioceramics: A Review of Their History, Structure, Properties, Coating Technologies and Biomedical Applications. Materials 2017; 10: 334.

8. Mondal S, Dorozhkin S V., Pal U. Recent progress on fabrication and drug delivery applications of nanostructured hydroxyapatite. Wiley Interdiscip Rev Nanomed Nanobiotechnol 2018; 10: e1504.

9. Xiao W, Sonny Bal B, Rahaman MN. Preparation of resorbable carbonate-substituted hollow hydroxyapatite microspheres and their evaluation in osseous defects in vivo. Materials Science and Engineering: C 2016; 60: 324–332.

10. Jeong J, Kim JH, Shim JH, Hwang NS, Heo CY. Bioactive calcium phosphate materials and applications in bone regeneration. Biomater Res 2019; 23.

11. Bhattacharjee MirinalK. Chemistry of antibiotics and related drugs. Cham: Springer., 2016.

12. Bidossi A, Bottagisio M, Logoluso N, De Vecchi E. In Vitro Evaluation of Gentamicin or Vancomycin Containing Bone Graft Substitute in the Prevention of Orthopedic Implant-Related Infections. Int J Mol Sci 2020; 21: 9250.

13. Tiwari A, Sharma P, Vishwamitra B, Singh G. Review on Surface Treatment for Implant Infection via Gentamicin and Antibiotic Releasing Coatings. Coatings 2021, Vol 11, Page 1006 2021; 11: 1006.

14. Al-Kuraishy H, Al-Gareeb A, Al-Nami M. Vinpocetine improves oxidative stress and pro-inflammatory mediators in acute kidney injury. Int J Prev Med 2019; 10: 142.

15. Dwivedi S, Saquib Q, Al-Khedhairy AA, Ahmad J, Siddiqui MA, Musarrat J. Rhamnolipids functionalized AgNPs-induced oxidative stress and modulation of toxicity pathway genes in cultured MCF-7 cells. Colloids Surf B Biointerfaces 2015; 132: 290–298.

16. Bharali P, Saikia JP, Ray A, Konwar BK. Rhamnolipid (RL) from Pseudomonas aeruginosa OBP1: A novel chemotaxis and antibacterial agent. Colloids Surf B Biointerfaces 2013; 103: 502–509.

17. Dai L, Li R, Wei Y, Sun C, Mao L, Gao Y. Fabrication of zein and rhamnolipid complex nanoparticles to enhance the stability and in vitro release of curcumin. Food Hydrocoll 2018; 77: 617–628.

18. Khalid HF, Tehseen B, Sarwar Y *et al.* Biosurfactant coated silver and iron oxide nanoparticles with enhanced anti-biofilm and anti-adhesive properties. J Hazard Mater 2019; 364: 441–448.

19. Tambone E, Bonomi E, Ghensi P *et al.* Rhamnolipid coating reduces microbial biofilm formation on titanium implants: an in vitro study. BMC Oral Health 2021; 21: 1–13.

20. Guzmán E, Ortega F, Rubio RG. Exploring the world of rhamnolipids: A critical review of their production, interfacial properties, and potential application. Curr Opin Colloid Interface Sci 2024; 69: 101780.

21. Gogia J, Meehan J, Di Cesare P, Jamali A. Local Antibiotic Therapy in Osteomyelitis. Semin Plast Surg 2009; 23: 100–107.

22. Martínez-Pastor JC, Muñoz-Mahamud E, Vilchez F *et al.* Outcome of Acute Prosthetic Joint Infections Due to Gram-Negative Bacilli Treated with Open Debridement and Retention of the Prosthesis. Antimicrob Agents Chemother 2009; 53: 4772–4777.

23. Kluin OS, Van Der Mei HC, Busscher HJ, Neut D. Biodegradable vs non-biodegradable antibiotic delivery devices in the treatment of osteomyelitis. Expert Opin Drug Deliv 2013; 10: 341–351.

24. Zimmerli W, Sendi P. Orthopaedic biofilm infections. APMIS 2017; 125: 353–364.

25. Ribeiro M, Monteiro FJ, Ferraz MP. Infection of orthopedic implants with emphasis on bacterial adhesion process and techniques used in studying bacterial-material interactions. Biomatter 2012; 2: 176–194.

26. Tao F, Ma S, Tao H *et al.* Chitosan-based drug delivery systems: From synthesis strategy to osteomyelitis treatment – A review. Carbohydr Polym 2021; 251: 117063.

27. Nandi SK, Mukherjee P, Roy S, Kundu B, De DK, Basu D. Local antibiotic delivery systems for the treatment of osteomyelitis – A review. Materials Science and Engineering: C 2009; 29: 2478–2485.

28. Kolmas J, Krukowski S, Laskus A, Jurkitewicz M. Synthetic hydroxyapatite in pharmaceutical applications. Ceram Int 2016; 42: 2472–2487.

29. Palazzo B, Iafisco M, Laforgia M *et al.* Biomimetic Hydroxyapatite–Drug Nanocrystals as Potential Bone Substitutes with Antitumor Drug Delivery Properties. Adv Funct Mater 2007; 17: 2180–2188.

30. Lai W, Chen C, Ren X, Lee IS, Jiang G, Kong X. Hydrothermal fabrication of porous hollow hydroxyapatite microspheres for a drug delivery system. Materials Science and Engineering: C 2016; 62: 166–172.

31. Long T, Guo Y-P, Liu Y-Z, Zhu Z-A. Hierarchically nanostructured mesoporous carbonated hydroxyapatite microspheres for drug delivery systems with high drug-loading capacity. RSC Adv 2013; 3: 24169.

32. Yu M, Zhou K, Li Z, Zhang D. Preparation, characterization and in vitro gentamicin release of porous HA microspheres. Materials Science and Engineering: C 2014; 45: 306–312.

33. Prasanna APS, Venkatasubbu GD. Sustained release of amoxicillin from hydroxyapatite nanocomposite for bone infections. Prog Biomater 2018; 7: 289–296.

34. Guo Y-J, Long T, Chen W, Ning C-Q, Zhu Z-A, Guo Y-P. Bactericidal property and biocompatibility of gentamicin-loaded mesoporous carbonated hydroxyapatite microspheres. Materials Science and Engineering: C 2013; 33: 3583–3591.

35. Wang S, Wang X, Xu H *et al.* Towards sustained delivery of small molecular drugs using hydroxyapatite microspheres as the vehicle. Advanced Powder Technology 2010; 21: 268–272.

36. Jiang J-L, Li Y-F, Fang T-L *et al.* Vancomycin-loaded nano-hydroxyapatite pellets to treat MRSA-induced chronic osteomyelitis with bone defect in rabbits. Inflammation Research 2012; 61: 207–215.

37. Jiang X, Zhang D, Sun R *et al.* A combined experimental and molecular dynamics simulation study on doxorubicin adsorption on strontium-substituted hydroxyapatite hollow microspheres. Appl Surf Sci 2021; 542: 148667.

38. Ma M-Y, Zhu Y-J, Li L, Cao S-W. Nanostructured porous hollow ellipsoidal capsules of hydroxyapatite and calcium silicate: preparation and application in drug delivery. J Mater Chem 2008; 18: 2722.

39. Safi S, Karimzadeh F, Labbaf S. Mesoporous and hollow hydroxyapatite nanostructured particles as a drug delivery vehicle for the local release of ibuprofen. Materials Science and Engineering: C 2018; 92: 712–719.

40. Munir MU, Ihsan A, Sarwar Y *et al.* Hollow mesoporous hydroxyapatite nanostructures; smart nanocarriers with high drug loading and controlled releasing features. Int J Pharm 2018; 544: 112–120.

41. Xu Q, Tanaka Y, Czernuszka JT. Encapsulation and release of a hydrophobic drug from hydroxyapatite coated liposomes. Biomaterials 2007; 28: 2687–2694.

42. Wu MY, Kao IF, Fu CY, Yen SK. Effects of Adding Chitosan on Drug Entrapment Efficiency and Release Duration for Paclitaxel-Loaded Hydroxyapatite—Gelatin Composite Microspheres. Pharmaceutics 2023, Vol 15, Page 2025 2023; 15: 2025.

43. Lee Y, Lee D, Park E *et al.* Rhamnolipid-coated W/O/W double emulsion nanoparticles for efficient delivery of doxorubicin/erlotinib and combination chemotherapy. J Nanobiotechnology 2021; 19: 1–13.

44. Wiegand I, Hilpert K, Hancock REW. Agar and broth dilution methods to determine the minimal inhibitory concentration (MIC) of antimicrobial substances. Nature Protocols 2008 3:2 2008; 3: 163–175.

45. Chen SF, Yu SH, Hang J, Li F, Liu Y. Polymorph discrimination of CaCO3 mineral in an ethanol/water solution: Formation of complex vaterite superstructures and aragonite rods. Chemistry of Materials 2006; 18: 115–122.

46. Chong KY, Chia CH, Zakaria S, Sajab MS. Vaterite calcium carbonate for the adsorption of Congo red from aqueous solutions. J Environ Chem Eng 2014; 2: 2156–2161.

47. Ševčík R, Pérez-Estébanez M, Viani A, Šašek P, Mácová P. Characterization of vaterite synthesized at various temperatures and stirring velocities without use of additives. Powder Technol 2015; 284: 265–271.

48. Zhao D, Jiang J, Xu J, Yang L, Song T, Zhang P. Synthesis of template-free hollow vaterite CaCO3 microspheres in the H2O/EG system. Mater Lett 2013; 104: 28–30.

49. Buljan Meić I, Kontrec J, Domazet Jurašin D *et al.* How similar are amorphous calcium carbonate and calcium phosphate? A comparative study of amorphous phase formation conditions. CrystEngComm 2018; 20: 35–50.

50. Lin K, Chen L, Liu P *et al.* Hollow magnetic hydroxyapatite microspheres with hierarchically mesoporous microstructure for pH-responsive drug delivery. CrystEngComm 2013; 15: 2999.

51. Goloshchapov DL, Kashkarov VM, Rumyantseva NA *et al.* Synthesis of nanocrystalline hydroxyapatite by precipitation using hen’s eggshell. Ceram Int 2013; 39: 4539–4549.

52. Qiao W, Lan X, Tsoi JKH *et al.* Biomimetic hollow mesoporous hydroxyapatite microsphere with controlled morphology, entrapment efficiency and degradability for cancer therapy. RSC Adv 2017; 7: 44788–44798.

53. Boskey AL, Robey PG. The Composition of Bone. Primer on the Metabolic Bone Diseases and Disorders of Mineral Metabolism: Eighth Edition 2013; 49–58.

54. Landi E, Celotti G, Logroscino G, Tampieri A. Carbonated hydroxyapatite as bone substitute. J Eur Ceram Soc 2003; 23: 2931–2937.

55. Krajewski A, Mazzocchi M, Buldini PL *et al.* Synthesis of carbonated hydroxyapatites: efficiency of the substitution and critical evaluation of analytical methods. J Mol Struct 2005; 744–747: 221–228.

56. Calasans-Maia MD, de Melo BR, Alves ATNN *et al.* Cytocompatibility and biocompatibility of nanostructured carbonated hydroxyapatite spheres for bone repair. Journal of Applied Oral Science 2015; 23: 599–608.

57. Rehman I, Bonfield W. Characterization of hydroxyapatite and carbonated apatite by photo acoustic FTIR spectroscopy. J Mater Sci Mater Med 1997; 8: 1–4.

58. Ren F, Ding Y, Leng Y. Infrared spectroscopic characterization of carbonated apatite: A combined experimental and computational study. J Biomed Mater Res A 2014; 102: 496–505.

59. Ji J, Hao S, Wu D, Huang R, Xu Y. Preparation, characterization and in vitro release of chitosan nanoparticles loaded with gentamicin and salicylic acid. Carbohydr Polym 2011; 85: 803–808.

60. María González González JCC and JB. Preparation and Characterization of PVDF. INTECH Open Access Publisher, 2012.

61. Talari ACS, Martinez MAG, Movasaghi Z, Rehman S, Rehman IU. Advances in Fourier transform infrared (FTIR) spectroscopy of biological tissues. Appl Spectrosc Rev 2017;

62. Nabipour H, Soltani B, Ahmadi Nasab N. Gentamicin Loaded Zn2(bdc)2(dabco) Frameworks as Efficient Materials for Drug Delivery and Antibacterial Activity. J Inorg Organomet Polym Mater 2018; 28: 1206–1213.

63. Batul R, Bhave M, Mahon PJ, Yu A. Polydopamine Nanosphere with In-Situ Loaded Gentamicin and Its Antimicrobial Activity. Molecules 2020, Vol 25, Page 2090 2020; 25: 2090.

64. Ţucureanu V, Matei A, Avram AM. FTIR Spectroscopy for Carbon Family Study. Crit Rev Anal Chem 2016; 46: 502–520.

65. Niaz T, Shabbir S, Noor T, Imran M. Antimicrobial and antibiofilm potential of bacteriocin loaded nano-vesicles functionalized with rhamnolipids against foodborne pathogens. LWT 2019; 116: 108583.